

Article

Pore Characteristics of Hydrate-Bearing Sediments from Krishna-Godavari Basin, Offshore India

Wen Guan ¹, Hailin Yang ¹ , Xindi Lu ² and Hailong Lu ^{1,3,4,*}

¹ Beijing International Center for Gas Hydrate, School of Earth and Space Sciences, Peking University, Beijing 100871, China; 2001110630@pku.edu.cn (W.G.); hyang@pku.edu.cn (H.Y.)

² Peking University Shenzhen Graduate School, Shenzhen 518055, China; luxindi@pku.edu.cn

³ Technology Innovation Center for Carbon Sequestration and Geological Energy Storage, MNR, Beijing 100091, China

⁴ National Engineering Research Center for Gas Hydrate Exploration and Development, Guangzhou 511466, China

* Correspondence: hlu@pku.edu.cn

Abstract: Pore-filling hydrates are the main occurrence forms of marine gas hydrates. Pore characteristics are a vital factor affecting the thermodynamic properties of hydrates and their distribution in sediments. Currently, the characterization of the pore system for hydrate-bearing reservoirs are little reported. Therefore, this paper focuses on the Krishna-Godavari Basin, via various methods to characterize the hydrate-bearing sediments in the region. The results showed that X-ray diffraction (XRD) combined with scanning electron microscopy (SEM) and cast thin section (CTS) can better characterize the mineral composition in the reservoir, high-pressure mercury injection (HPMI) focused on the contribution of pore size to permeability, constant-rate mercury injection (CRMI) had the advantage of distinguishing between the pore space and pore throat, and nuclear magnetic resonance cryoporometry (NMRC) technique can not only obtain the pore size distribution of nanopores with a characterization range greater than nitrogen gas adsorption (N₂GA), but also quantitatively describe the trend of fluids in the pore system with temperature. In terms of the pore system, the KG Basin hydrate reservoir develops nanopores, with a relatively dispersed mineral distribution and high content of pyrite. Rich pyrite debris and foraminifera-rich paleontological shells are observed, which leads to the development of intergranular pores and provides more nanopores. The pore throat concentration and connectivity of the reservoir are high, and the permeability of sediments in the same layer varies greatly. The reason for this phenomenon is the significant difference in average pore radius and pore size contribution to pore permeability. This article provides a reference and guidance for exploring the thermodynamic stability of hydrates in sediments and the exploration and development of hydrates by characterizing the pores of hydrate reservoirs.

Keywords: hydrate-bearing sediments; microporous structure; Krishna-Godavari Basin; pore characterization



Citation: Guan, W.; Yang, H.; Lu, X.; Lu, H. Pore Characteristics of Hydrate-Bearing Sediments from Krishna-Godavari Basin, Offshore India. *J. Mar. Sci. Eng.* **2024**, *12*, 1717. <https://doi.org/10.3390/jmse12101717>

Academic Editor: Manuel Martín-Martín

Received: 17 August 2024

Revised: 16 September 2024

Accepted: 26 September 2024

Published: 29 September 2024



Copyright: © 2024 by the authors. Licensee MDPI, Basel, Switzerland. This article is an open access article distributed under the terms and conditions of the Creative Commons Attribution (CC BY) license (<https://creativecommons.org/licenses/by/4.0/>).

1. Introduction

As an important natural gas resource, hydrate-bearing sediment reservoirs have attracted extensive attention in recent years. Due to their unique physical and chemical properties, the microscopic pore structure of hydrate-bearing sediments has a decisive impact on their reserves and exploitation efficiency [1–3]. The pore-filling hydrate is the main storage form of marine gas hydrates, and pore features are important factors affecting the thermodynamic properties of the hydrate and its distribution in sediments, and the pore diameter, pore size distribution, pore connectivity, and physicochemical properties of pore surface are the key factors determining the formation, decomposition, and migration of the hydrate [4–7].

The properties of reservoirs, as key factors affecting the behavior of underground fluids and the occurrence of resources, have a profound impact on the formation and distribution of hydrates due to their various characteristics. Specifically, the following properties are particularly crucial:

Permeability is a physical parameter that measures the ability of a reservoir rock to allow fluid to pass through its pore space. A high permeability reservoir means that fluids (including water and gas) can flow more freely, which helps the raw materials for hydrate formation—gases (such as methane)—to more effectively contact and react with water, thereby promoting the formation of hydrates. On the contrary, low-permeability areas may suppress the widespread distribution of hydrates due to the restricted fluid flow.

Porosity reflects the proportion of pore volume to total volume in a reservoir, directly related to the reservoir's ability to accommodate fluids (including the water and gas required for hydrate formation). A higher porosity not only provides more space for the formation of hydrates, but also promotes fluid interactions, which is beneficial for the formation of hydrates. On the contrary, reservoirs with a low porosity typically have limited potential for hydrate formation.

The organic matter in the reservoir, especially those that can decompose to produce gas, has an indirect but important impact on the formation of hydrates. The decomposition process of organic matter releases gases such as methane, which are the main components of natural gas hydrates. Therefore, reservoirs with abundant organic matter often have superior conditions for hydrate formation.

The mineral composition of a reservoir not only affects its physical properties such as permeability and pore structure, but may also affect the stability of hydrates through chemical reactions. The surface properties of certain minerals (such as clay minerals) may promote or hinder the growth of hydrate crystals, and certain specific mineral combinations may also provide more stable attachment points for hydrates, thereby affecting their distribution patterns. In addition, trace elements in minerals may also have subtle effects on the formation conditions of hydrates.

The properties of reservoir permeability, porosity, organic matter content, and mineral composition, which directly or indirectly affect the formation and distribution of hydrates, are key factors that must be carefully considered when studying and predicting hydrate resources.

However, the extraction and utilization of gas hydrates face several technical challenges, one of which is the in-depth understanding and characterization of the microscopic pore structure of the reservoir. In addition, the properties of the reservoir (e.g., permeability, porosity, organic matter content, mineral composition, etc.) also have a significant impact on the formation and distribution of hydrates [8,9]. Limited to characterization methods, the characterization of microscopic pore structure systems of hydrate-bearing sediment reservoirs is rarely reported. Due to the complex pore structure and variable reservoir conditions, how to accurately characterize microscopic pores has always been a research problem in this field. Therefore, this study focuses on the sediment system characterization of the KG Basin in the gas-hydrate-bearing region of India.

The Krishna-Godavari (KG) Basin in India is one of the world's largest gas hydrate deposits, with low permeability and high saturation reservoir characteristics, making hydrate extraction and utilization challenging [10–12]. The study of the characteristics of the reservoir, especially the study of the microporous structure, not only helps to better understand the storage state of hydrates, but also provides an important theoretical basis for subsequent exploration technology, which is essential for the effective development and utilization of hydrate resources.

Scholars have used the HPMI and N₂GA methods to characterize the porosity of the KG Basin [13,14]. Daigle et al. used the HPMI method to study the microporous system of hydrate-bearing sediments in the Kumano Basin off the coast of Japan, and found that micron-scale pores led to the uplift of the methane hydrate stability zone (MHSZ) basement, showing the effect of pore size on MHSZ thickness. In another study, Daigle et al.

performed nitrogen adsorption (N_2 GA) experiments to determine the pore size distribution (PSD) of nanoscale pores by the Barrett–Joiner–Halenda (BJH) model and merge them with the HPMI data. The results showed that the micropore content (with a pore size of less than 2 nm) was mainly affected by mineralogy, and the diagenesis process also had a certain influence. The micropore content was mainly determined by the abundance of detrital clay and the development process of clay as an ash alteration product, and the amorphous silica cement precipitated in areas with an abnormally high porosity also had a certain effect.

However, there is no systematic study on the microscopic porosity of hydrate-bearing sediment reservoirs in the KG Basin, and the characterization methods used are relatively single, and the applicability of other methods in the characterization of hydrate-bearing reservoirs is not clear. Due to the complexity and particularity of the geological conditions of the hydrate-bearing sediment reservoirs in the KG Basin, there are still many challenges in the in-depth research and effective development and utilization of the reservoirs.

The characterization of hydrate containing sediments is of great significance from multiple perspectives such as energy, environmental implications, and geohazards.

From an energy perspective, it helps to evaluate the development potential of natural gas hydrates. Understanding and characterizing the properties of hydrate-containing sediments is crucial for assessing their energy development potential. By conducting in-depth research on the physical, chemical, and mechanical properties of hydrate-containing sediments, a scientific basis and technical support can be provided for their safe and efficient mining.

From the perspective of environmental implications, it is related to the balance of marine ecosystems and the response to global climate change. Submarine sediments are an important component of marine ecosystems, containing abundant organic matter and microorganisms that provide nutrients and energy for the ecosystem. The thermodynamic stability of sediment containing hydrates is directly related to the balance of marine ecosystems. Once hydrates are decomposed or improperly extracted, they may disrupt the stability of seabed sediments, thereby affecting the health and stability of marine ecosystems. In addition, when external conditions do not meet the thermodynamic stability conditions of hydrates, they may decompose and release greenhouse gases such as methane under specific conditions. Understanding and characterizing the stability of hydrate containing sediments is of great significance for assessing their potential greenhouse gas emission risks. Through scientific research and effective management, the impact of hydrate sediment decomposition on global climate change can be minimized to the greatest extent possible.

From the perspective of geohazards, it helps to assess risks such as ground subsidence and groundwater pollution. The ground subsidence risk is described as follows: The thermodynamic temperature and pressure changes of sediment containing hydrates may lead to geological hazards such as ground subsidence. For example, in the process of natural gas hydrate extraction, if the stability of hydrate containing sediments is not effectively controlled, factors such as changes in pore water pressure may cause the plastic deformation of the soil layer, leading to ground subsidence. Understanding and characterizing the mechanical properties of hydrate-containing sediments is of great significance for assessing their geological hazard risk. Secondly, sediment containing hydrates may contain harmful substances such as heavy metals and organic pollutants. If hydrates are decomposed or extracted improperly, it may lead to the release of these harmful substances into groundwater, causing pollution of the groundwater. By characterizing the pollutant content and migration transformation patterns of sediment containing hydrates, a scientific basis and technical support can be provided for its pollution prevention and control [15,16].

In order to overcome the above shortcomings and better understand the microscopic pore structure of hydrate-bearing sediment reservoirs, this study took the hydrate-bearing reservoirs in the KG Basin as the research object, explored the applicability of various characterization techniques, compared the advantages and limitations of qualitative and quantitative characterization techniques, and analyzed the microporous structure and

heterogeneity of hydrate-bearing sediment. This study not only helps to deepen the understanding of the micropores of hydrate-bearing reservoirs, but also provides a scientific basis for the characterization of hydrate-bearing reservoirs in other regions, and provides an important reference for parameter setting and the exploration and exploitation of hydrates, which will promote the further development of the research field of hydrate-bearing reservoirs.

2. Geological Background

The Krishna-Godavari Basin (Figure 1) is a sedimentary basin on the Indian subcontinent whose formation is closely related to the collision of the Indian Plate with the Eurasian Plate and the subsequent tectonic activity. Over the course of its geological history, the KG Basin has undergone numerous transgressions and retreats, resulting in a variety of sedimentary facies zones and sedimentary systems. The interior of the basin is mainly composed of Paleozoic and Mesozoic sedimentary strata, which are rich in organic matter, which provides a material basis for oil and gas generation. Changes in sedimentary facies zones and sedimentary systems not only control the formation and aggregation of hydrocarbons, but also affect the development of reservoirs and caprocks. Sediments have a significant influence on the formation of hydrates in the Krishna-Godavari Basin, and the lithology, organic matter content, pore water, and fluid migration characteristics of sediments, and the correlation with hydrate saturation are all responsible for the formation and distribution of gas hydrates.

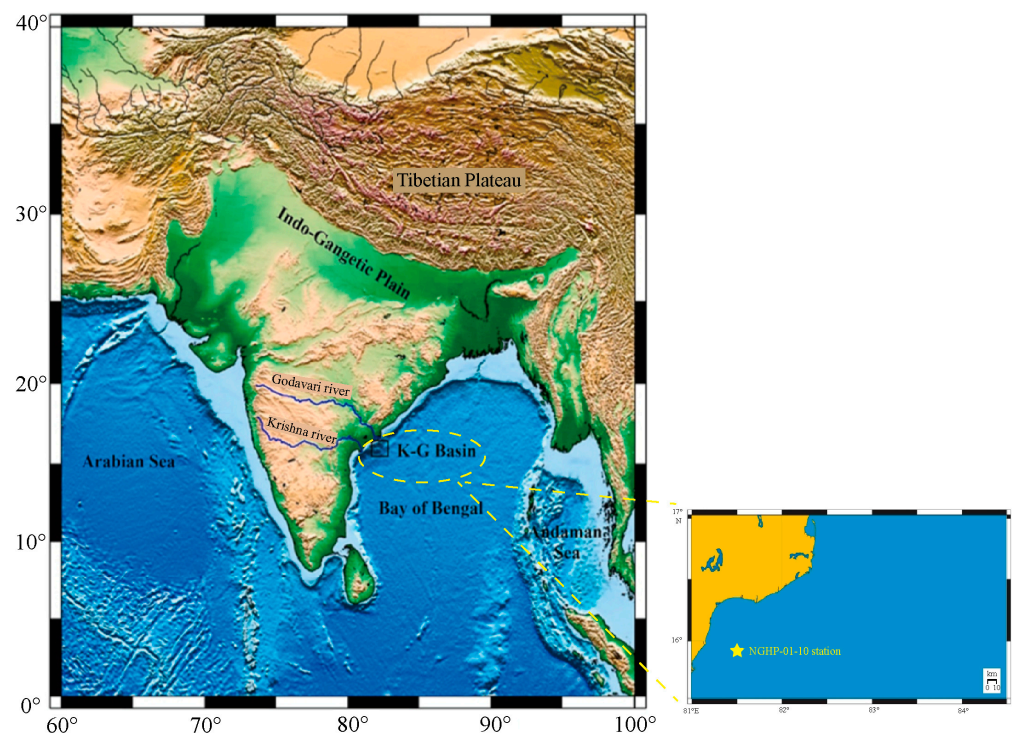


Figure 1. Schematic diagram of the geographical location of the KG Basin and the station location of NGHP-01-10.

The lithology of sediments directly determines their pore structure, permeability, and storage space. Generally speaking, sediments with a large porosity, coarse grains, and high sedimentation rate are conducive to the formation of hydrates. In the KG Basin, different types of sediments, such as mudstone, silty mudstone, sandstone, etc., have different pore structures and hydrogeological conditions, which affect the formation and distribution of hydrates.

The organic matter content in sediments is an important material basis for the formation of gas hydrates. Organic matter can produce gases such as methane under the action of microorganisms, which are necessary for the formation of gas hydrates. As an important oil-bearing basin, the KG Basin is rich in organic matter in its sediments, which provides a sufficient gas source for the formation of gas hydrates.

The pore water in the sediment is not only an important medium for the formation of gas hydrates, but also transports methane and other gases to suitable accumulation sites through fluid transport. Tectonic activities such as faults and folds not only provide channels for the migration of underground fluids, but also indirectly affect the formation and distribution of hydrates by changing the pore structure and permeability of sediments [17–21].

Samples for this study were obtained from the KG Basin offshore India, which is located on the east coast of India and extends 500 km laterally and more than 200 km from the coast to the deep sea. The basin covers an area of 70,000 km², mostly alluvium, and 42,000 km² of offshore, mainly in the Bay of Bengal. India has launched a National Gas Hydrate Project (NGHP) in the KG Basin and discovered one of the richest marine gas hydrate aggregates, NGHP-01, with samples from station 01-10D (10X, cc), which is located between 15–16° N latitude and 81–82° E longitude [2,10,11,17,22].

3. Samples and Methodology

3.1. Sample Information

The hydrate-bearing sediments in the KG Basin are mainly composed of fine-grained sediments, and the particle size, composition, and distribution characteristics of the sediments are affected by a variety of factors, including tectonic activities within the basin, sedimentary environment, and sea level changes.

Experimental samples (Figure 2) were taken from station NGHP01-10-10D; after drilling and coring, the core sediments are preserved in liquid nitrogen tanks, and the sediments were mainly stripped from the Quaternary mudstones; grain size analysis showed that the grain size of the sediments was mainly sandy and silty; and the color of the sediment is predominantly black to grayish-black. In this study, two samples were tested with labels HYD58 and HYD68, respectively.

3.2. Experiments

The experimental process first formed a preliminary understanding of the physical characteristics of the reservoir by casting thin sections, X-ray diffraction (XRD), and particle size analysis, and obtained the specific data of the minerals in the reservoir, and then carried out field emission scanning electron microscopy (FESEM) and CTS method to obtain the 2D plane and 3D distribution of the pore and pore throat of the sample, to study the microscopic characteristics of the pore. Finally, on this basis, the NMRC method was tried to quantitatively characterize the nanoscale pores combined with N₂GA, and the applicability, advantages, and limitations of the two methods were compared through experimental data. HPMI and CRMI were used to quantitatively characterize the distribution characteristics of pores and throat.

3.2.1. XRD

Different mineral crystals correspond to different XRD patterns, and the intensity of the characteristic peaks in the spectrum is positively correlated with the mineral content in the sample, and the quantitative analysis is based on the “K-value method” [2,23,24].

Grind the sample into powder, fill the powder into glass sheets using the compression method, and then place the glass sheets into the instrument. Conduct experiments by setting parameters through software. The experiments were performed using the Netherlands PANalytical Empyrean Ray Diffractometer and the PIXcel1D-Medipix 3 detector (Malvern Panalytical Ltd.) with a scan step of 0.01° and copper K-α radiation. The measured XRD patterns were analyzed using MDI Jade 6.5 software.

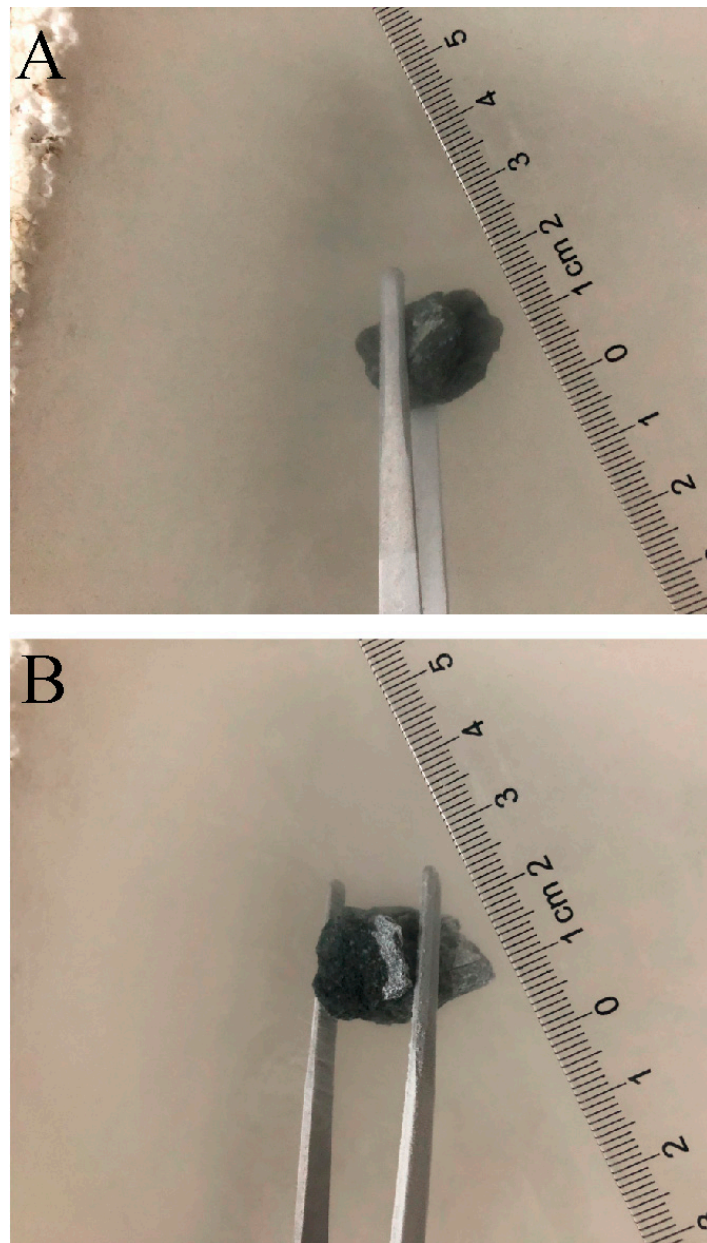


Figure 2. Sample sample 58 (A) and 68 (B) from NGHP-01-10.

3.2.2. CTS and SEM

Cast thin sections were cast using dye resins and then observed using a microscope to determine pore types and pore morphological characteristics at the micrometer scale.

Electron microscope samples are glued to the sample stage using electrostatic glue, gold-plated on a fresh plane of the sample using an ion-sputtering instrument, then analyzed using SEM to characterize pore types and morphology at the nanoscale level [25,26].

3.2.3. NMRC

The pore size affects the freezing point of the liquid in porous media, which can be quantitatively expressed by the Gibbs–Thomson equation [27–31].

The relationship between the melting point depression temperature (ΔT_m) and pore diameter (x) is as follows:

$$\Delta T_m = T_m - T_m(x) = \frac{4\sigma T_m}{x\rho\Delta H} \quad (1)$$

where x is diameter of the equivalent spherical pore, nm; ΔT_m is liquid melting point depression, K; T_m is melting point of the bulk material, K; $T_m(x)$ is melting point of a crystal, K; ΔH is bulk enthalpy of fusion, J/g; ρ is density of the solid, g/cm³; and σ is solid–liquid surface, N/m.

Generally, the σ , T_m , ρ , and ΔH can be regarded as constant; therefore, Equation (1) can be written as follows:

$$\Delta T_m = \frac{k_{GT}}{x} \tag{2}$$

where k_{GT} is Gibbs–Thomson constant, nm·K.

The formula with pore volume is given below:

$$P(x) = \frac{dv(x)}{dx} = \frac{dv(x)}{dT_m(x)} \times \frac{dT_m(x)}{dx} = \frac{dv(x)}{dT_m(x)} \times \frac{k_{GT}}{x^2} \tag{3}$$

The log differential PSD is calculated as follows:

$$\frac{dv(x)}{d\log(D)} = \frac{dv(x)}{dx} \times \frac{dx}{d\log(D)} = P(x) \cdot x \cdot \ln(10) \tag{4}$$

where x is the pore diameter, v is the volume of the water, and T is the temperature.

The NMRC method is used to record the phase transition process of hydrogen-containing fluids in porous media with temperature by NMR signals, and the increase in the signal of low-temperature liquids means that the pore volume is accumulated from small to large. In this research, experiments were performed using the NMR MesoMR23-060V-1 (Suzhou Niumag Analytical Instruments Co.); we choose water as liquid probe with a temperature range of −30 °C to 25 °C.

3.2.4. HPMI

The experiment was used Micromeritics Auto Pore IV 9505 mercury injection meter with a mercury injection pressure range of 0–200 MPa. After drying the sample, calibrate the instrument, set the test parameters, and load the sample into the sample chamber for experimentation.

The structural characteristics of the pore and throat were analyzed according to the Washburn equation, and the mercury injection pressure curve was transformed by the following [32]:

$$P_c = \frac{2\sigma \cos \theta}{r} \tag{5}$$

where P_c is capillary pressure, MPa; θ is wetting angle, $\theta = 140^\circ$; σ is surface tension, N/m, $\sigma = 0.48$ N/m, and r is pore diameter.

3.2.5. CRMI

The experiment used ASPE730 system to monitor mercury injection with the maximum injection pressure of 900 psi and the constant rate of mercury injection velocity of 0.0001 mL/min; the constant low velocity allows the mercury introductory process to be approximated as a quasi-static process. During this process, the interfacial tension and contact angle remain constant, and every change in pore shape experienced by the leading edge of the mercury causes a change in the capillary pressure of the system; the pores and throats identified by pressure fluctuations during mercury injection.

3.2.6. LP-N₂GA

The samples were prepared as powders (60–80 mesh), dried to remove residual liquid from the pores, and degassed for 12 h at room temperature. Then, using the Micromeritics ASAP 2460 device (Micromeritics Instruments Corporation), at the temperature of liquid nitrogen, the pressure was increased to achieve the saturated vapor pressure of the liquid nitrogen, and then the pressure was lowered to obtain the nitrogen adsorption–desorption curve.

The analysis of the specific surface area (SSA) and pore size distribution (PSD) is based on Brunauer–Emmett–Taylor (BET) and Barrett–Joyner–Hallenda (BJH) theories [33–35].

The experimental procedure is as follows: open the computer, vacuum pump, and adsorption instrument host in sequence, and enter the software operation interface. Then open the gas cylinder and adjust the pressure. Next, weigh the mass of the empty sample tube and plug, place the weighed sample into the already weighed empty sample tube, and degas the sample tube. After the processing time is reached, the temperature decreases to room temperature, backfill with gas, and weigh the mass of the sample, sample tube, and plug. Finally, use software operation program settings for sample analysis.

4. Results and Discussion

4.1. Mineral Compositions That Make Up the Pores

The study shows that the samples from the KG Basin mainly contained quartz, feldspar, calcite, pyrite, and a large number of clay minerals (Figure 3). The clay mineral content is the highest, with 45.3% and 37.9% in Samples 58 and 68, respectively. Clay minerals are widely developed in the illite/smectite mixed layer, with minor amounts of illite, kaolinite, and chlorite. In addition to clay minerals (Figure 4), the quartz content was higher, with Samples 58 and 68 containing 26.3% and 28.6%, respectively. Pyrite was also observed in the samples collected from the KG Basin, with Sample 68 having a higher percentage of pyrite at 10.1%, which may account for the high magnetic induction intensity observed here.

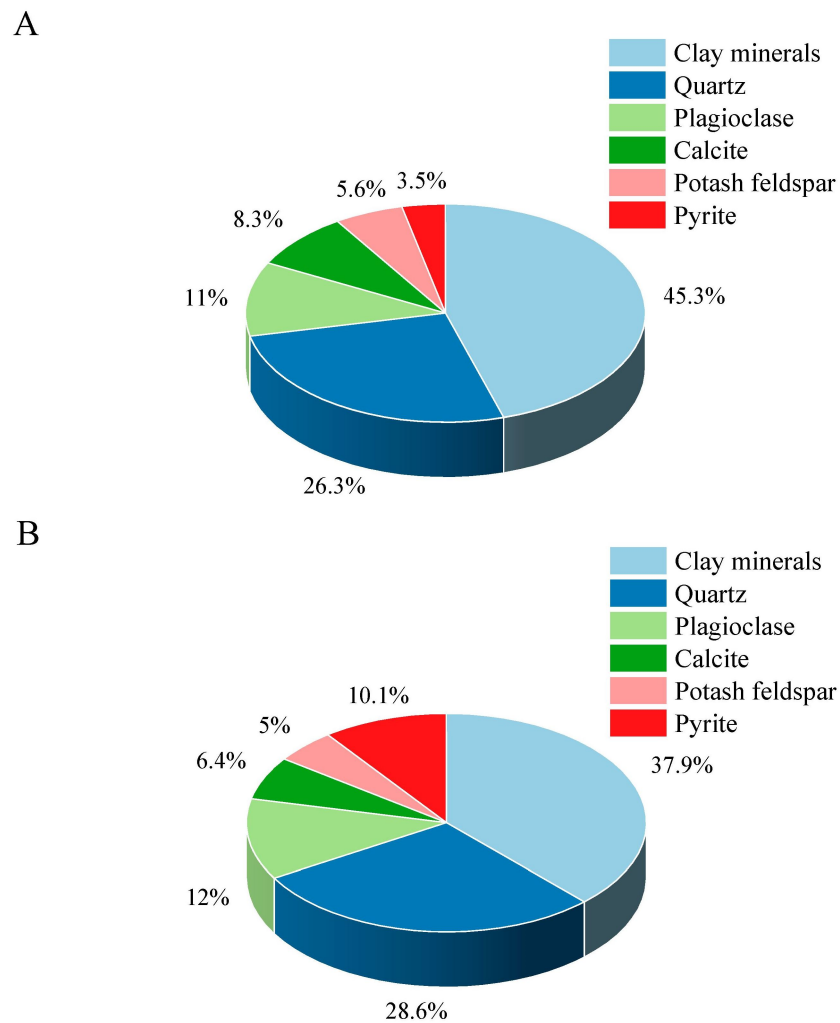


Figure 3. Pie charts of mineral content in Samples 58 and 68 ((A) Sample 58 and (B) Sample 68): (A) mineral content of Sample 58; and (B) mineral content of Sample 68.

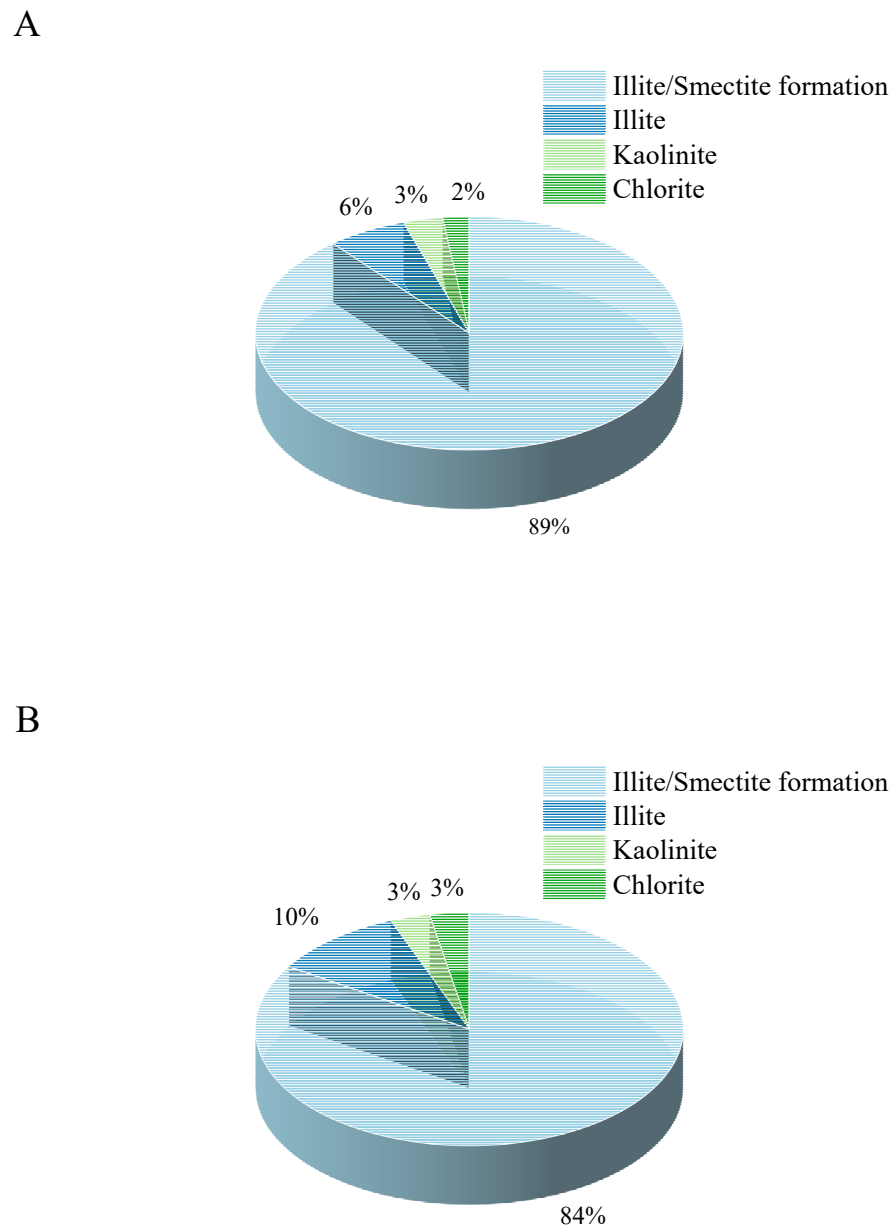


Figure 4. Pie charts of clay mineral content in Samples 58 and 68 ((**A**) Sample 58 and (**B**) Sample 68): (**A**) clay mineral content of Sample 58; and (**B**) clay mineral content of Sample 68.

Microscopic images of CTS show that the distribution of detrital minerals in both samples is relatively dispersed, with quartz and feldspar minerals being dominant (Figures 5 and 6). The particle sizes of the mineral grains are of micrometer scale, with none exceeding 100 μm . Nanoscale intergranular pores are formed between different minerals.

4.2. Pore and Throat Types, and Geometry

A microscopic observation of the sample revealed the presence of intergranular pores, intragranular pores, and microfractures (MFs). Microfractures consist of intergranular fractures (InterFs) and intragranular fractures (IntraFs).

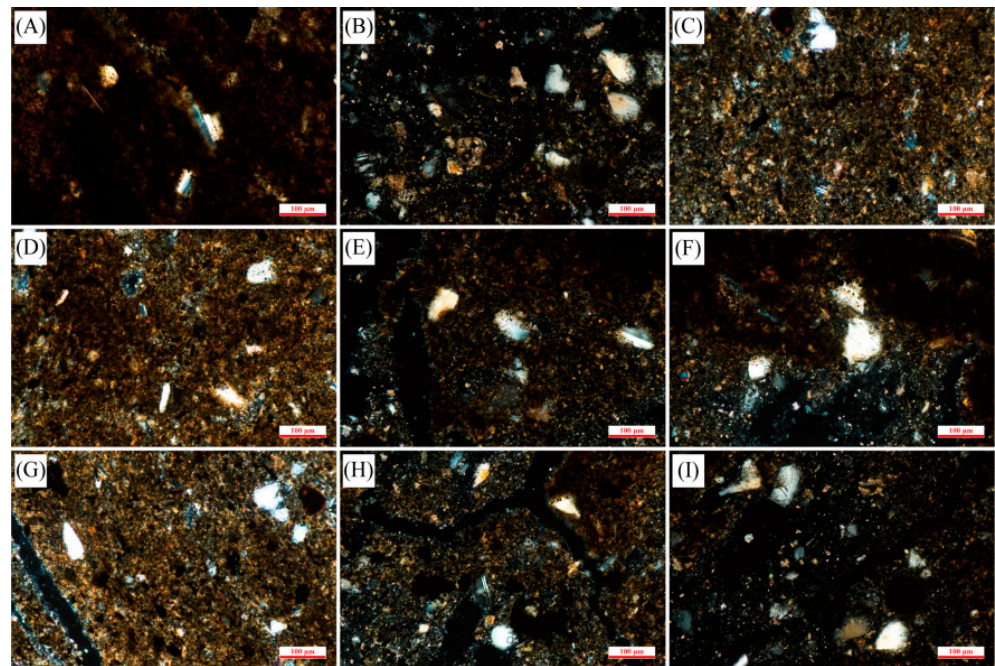


Figure 5. Microscopic observation of the mineral distribution in the CTS in Sample 58. (A): mainly feldspar; (B): mainly foraminiferal debris and quartz; (C): larger quartz and tiny feldspar; (D): quartz with different shapes; (E): quartz and feldspar; (F): quartz and feldspar; (G): quartz with different shapes; (H): larger quartz surrounded by tiny feldspar; (I) quartz with different shapes.

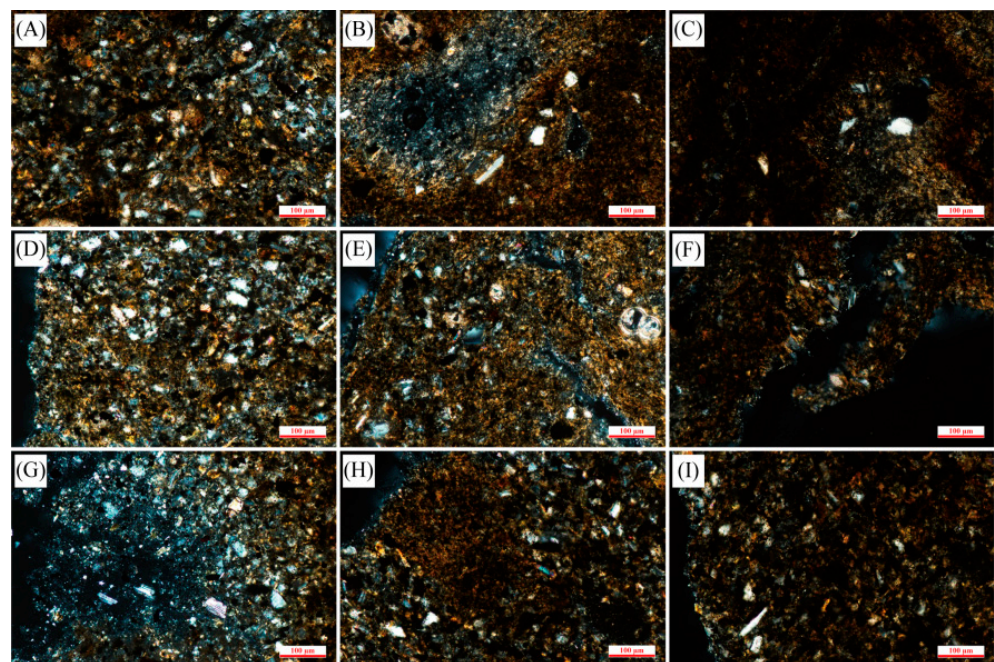


Figure 6. Microscopic observation of the mineral distribution in the CTS in Sample 68. (A): predominant distribution of tiny quartz detritus; (B): quartz and feldspar; (C): feldspar; (D): predominant distribution of tiny quartz; (E): foraminiferal detritus with quartz and feldspar; (F): tiny quartz and feldspar; (G): predominant distribution of quartz with feldspar; (H): quartz; (I) quartz.

4.2.1. Intragranular Pore

In terms of micropores, the biodebris such as shells of different species of foraminifera and algae were observed from CTS (Figures 7 and 8), with a more complete preservation of the contours, and intact chambers could be seen in the foraminifera. The broken

foraminifera shells were filled with minerals and organic matter. The biodebris described above mainly provide intragranular pores.

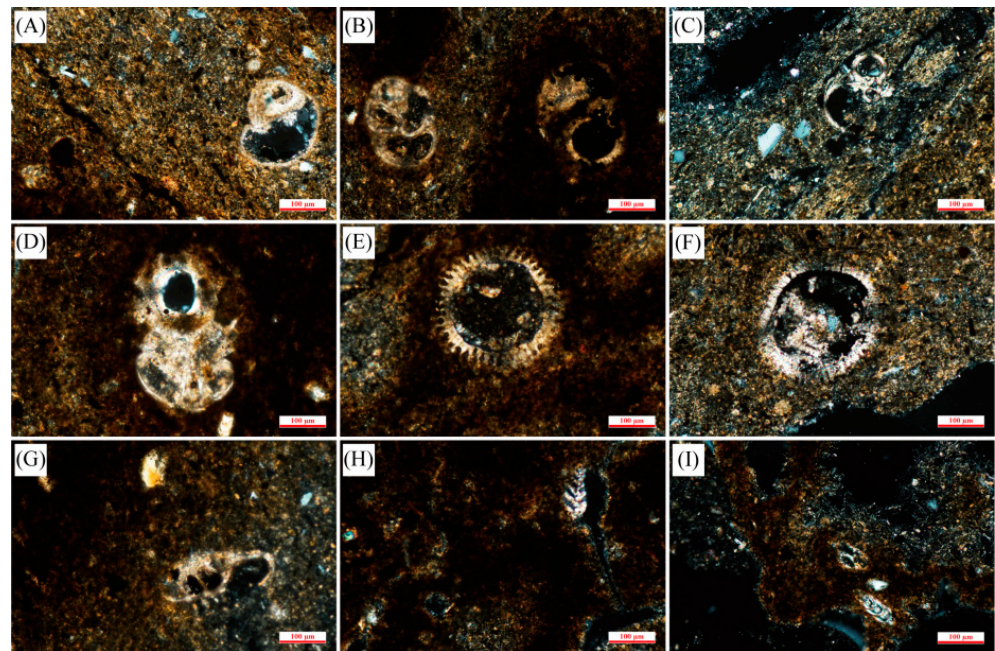


Figure 7. Microscopic observation of foraminiferal shells and diatom shells in CTS in Sample 58. (A): foraminiferal detritus; (B): foraminiferal detritus; (C): foraminiferal detritus; (D): foraminiferal detritus; (E): diatom detritus; (F): diatom detritus; (G): foraminiferal detritus; (H): foraminiferal detritus; (I) foraminiferal detritus.

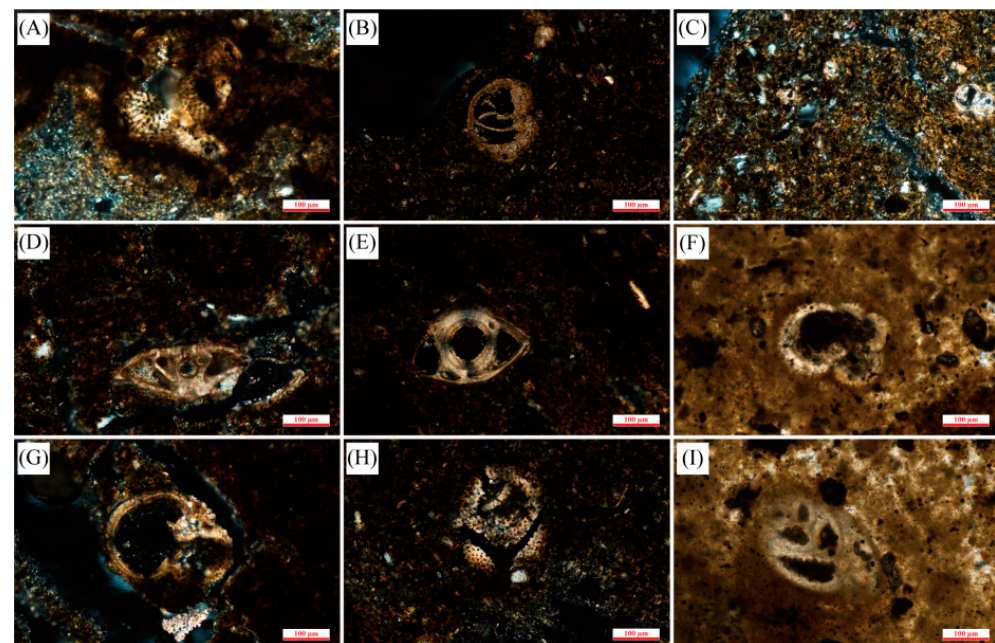


Figure 8. Microscopic observation of foraminiferal shells and diatom shells in CTS in Sample 68. (A): bioclasts with cellular structure; (B): foraminiferal detritus; (C): foraminiferal detritus; (D): diatom detritus; (E): diatom detritus; (F): diatom detritus; (G): foraminiferal detritus; (H): biodebris with cellular structure; (I) foraminiferal detritus.

Of course, this method has certain limitations. The mechanical polishing of sample pretreatment will cause an irregular surface morphology and difficulty distinguishing

pseudo-pores from true pores. Moreover, grinding particles can easily enter the actual pore area, resulting in the true pore being buried or obscured.

4.2.2. Intergranular Pore

Intergranular pores within the pyrite framboids were observed in SEM experiments on the nanoscale level (Figure 9); the accumulated particles were about 500 nm in diameter and uniform in size, mostly block hexahedral. Except pyrite framboids, pyrite mineral aggregates and intergranular pores were developed in the samples, which were contiguous and diffuse, and coexisted with clay minerals. The diameter of the pyrite grains in the aggregates varies widely, with most pyrite particles being around 600–800 nm in diameter and smaller pyrite particles of 70–250 nm in diameter stacked together.

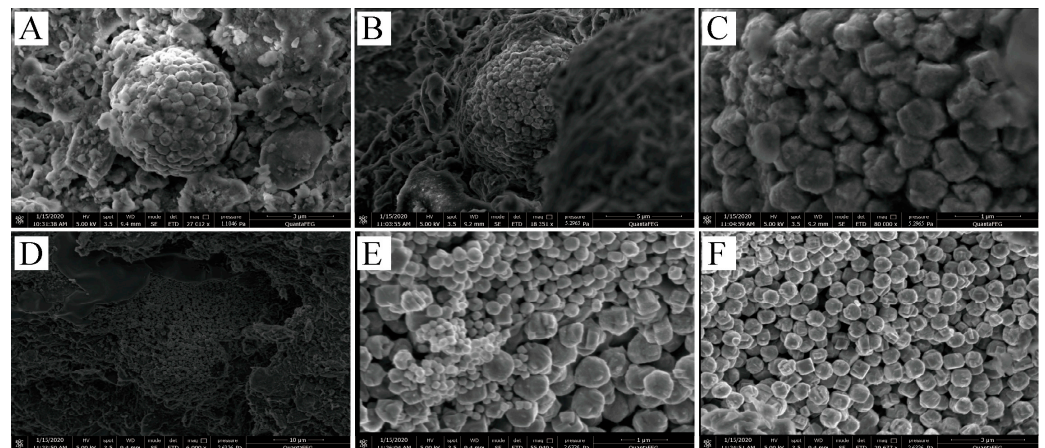


Figure 9. SEM observation of pyrite framboids in Sample 68. pyrite framboid in (A) main view; (B) side view; (C) detail view of pyrite particles; (D) pyrite aggregate; (E,F) detail view of pyrite particles of different diameters.

As for other minerals, illite is filled around mineral particles such as quartz and feldspar in the form of needles, flakes, and networks; the mineral particles and aggregates are stacked with each other to form a large number of micron-sized intergranular pores with complex morphologies. Kaolinite is a pseudo-hexagonal plate and worm-like, with a large number of intergranular pores. Rigid and brittle particles such as feldspar and quartz are accompanied by micro-cracks, and the width of the cracks is mostly 1–3 μm ; the surfaces are smooth and cracks are straight, and the extension distance is relatively far. Meanwhile, intragranular dissolved pores are observed in calcite.

4.2.3. Crack

The morphology of the bioclasts is preserved intact in the CTS, from which it can be inferred that the microcracks are non-artificial cracks with widths of a few micrometers. The cracks in Figure 10A,B are single microcracks without branching, and the crack in Figure 10C is connected to the bioclasts with multiple bifurcating microcracks, which increase the pore volume. The cracks in Figure 10D are not connected to the bioclasts, and the bioclast shells provide a certain closed-pore space.

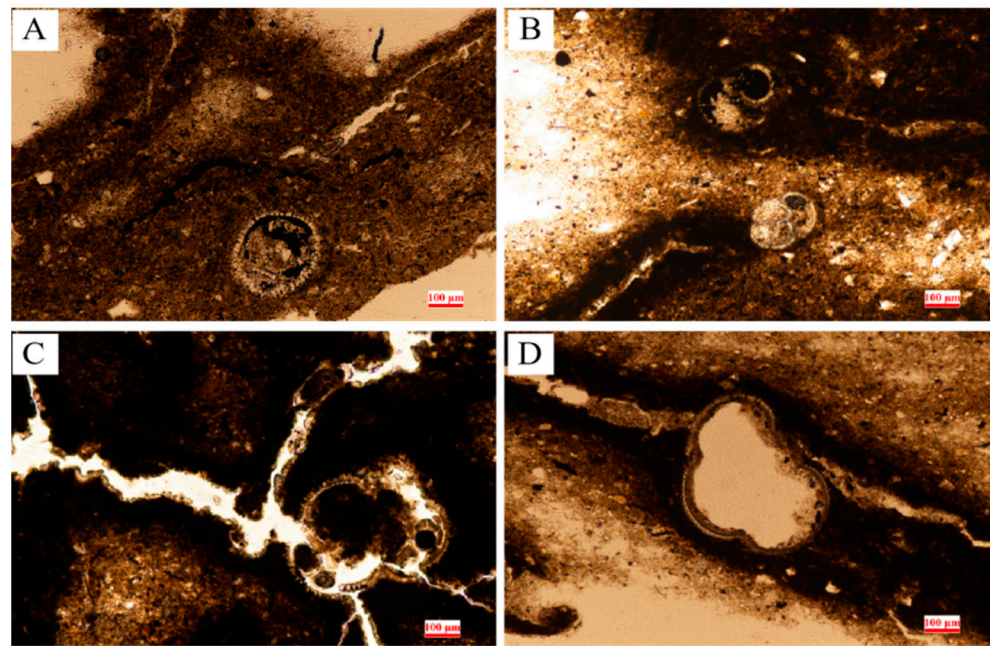


Figure 10. Microscopic observation of cracks in the CTS. (A,B): narrow microcracks; (C,D): wide microcracks.

4.3. Pore Size Distribution (PSD) and Connectivity

4.3.1. Nanometer-Scale Characterization—N₂GA

According to the classification of the International Union of Pure and Applied Chemistry (IUPAC), the characteristics of the pore structure can be analyzed by adsorption-desorption curves (Figure 11A) in the LP-N₂GA data. This process is divided into the following three stages:

1. In the part with a low relative pressure stage ($0 < P/P_0 < 0.4$), the adsorption capacity increases slowly, and the adsorption isothermal curve showed a slightly upward and convex shape. This stage was the transition process from mono-molecular layer adsorption to multi-molecular layer adsorption, and the inflection point of the isothermal adsorption curve was the critical point of the transition shift.

2. At the medium and high relative pressure stage ($0.4 < P/P_0 < 0.8$), the adsorption capacity increases slowly with the increase in pressure, and this stage is the multilayer adsorption process.

3. In the high relative pressure stage ($0.8 < P/P_0 < 1$), the adsorption isotherm rises sharply, showing a downward concave shape, and the adsorption saturation phenomenon does not occur until it is close to the saturation vapor pressure, which indicated that there existed a certain amount of macropores and mesopores in the sediment, resulting in the capillary condensation of nitrogen on the surface of the sediment sample.

According to IUPAC's classification, the adsorption isotherm of the samples is very steep near the saturated vapor pressure, close to type H3, while having the characteristics of type H4. These types of hysteresis line indicate that the sediment sampled are predominantly slit-type pores, but also contain some ink-bottle-shaped pores [36–38].

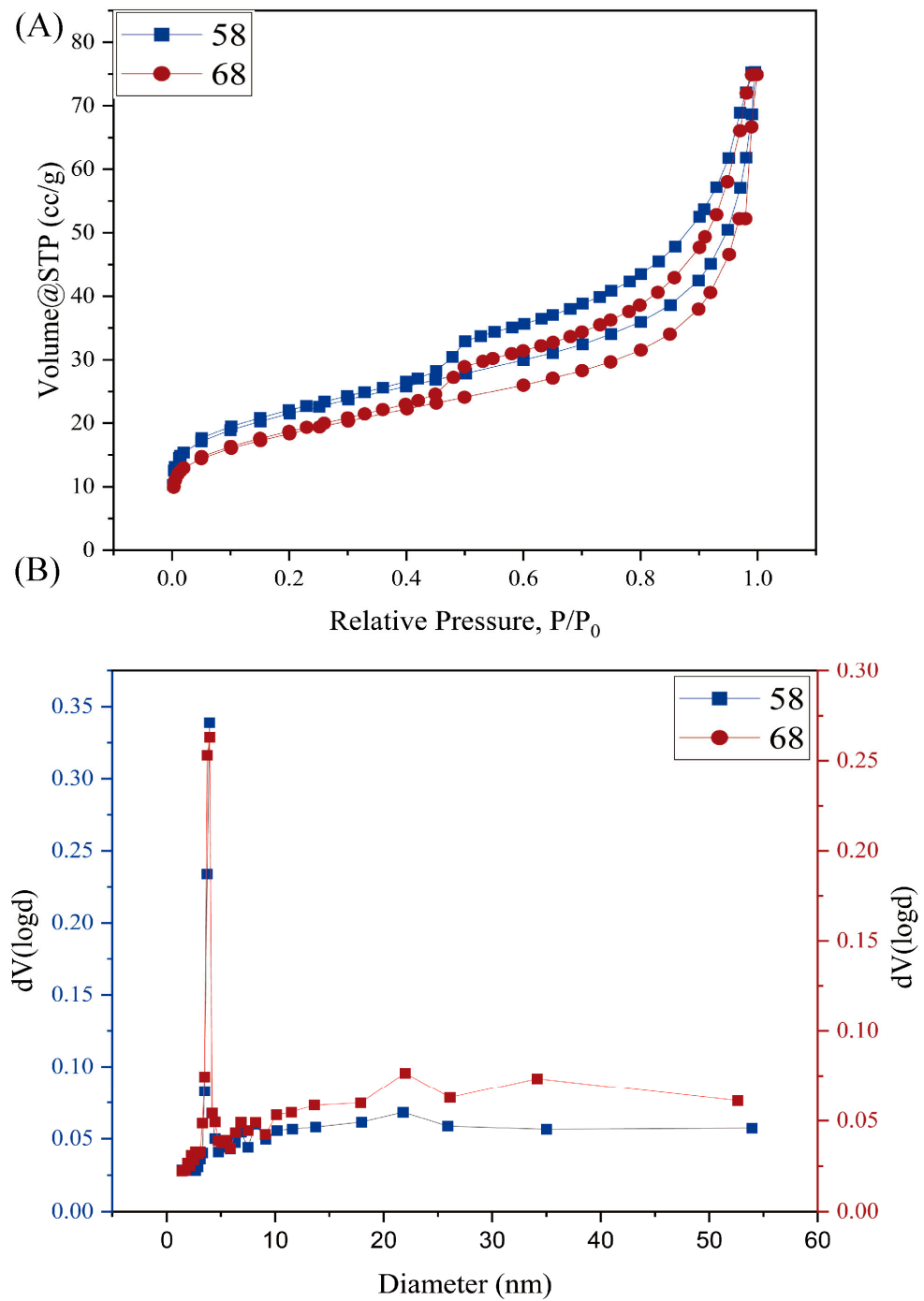


Figure 11. N₂GA isotherms (A) and pore size distributions (B). Figure (B) is a double Y-axis diagram, in which the left and right sides of the ordinate correspond to Samples 58 and 68, respectively.

4.3.2. Nanometer-Scale Characterization—NMRC

NMR T₂ spectrums are as follows:

Figures 12 and 13 show all the temperature points we set, as well as the acquired relaxation time T₂ spectrum. The experimental results show that the melting point of ice in the reservoir micropores is related to the pore size. Figures 14 and 15 show that, between −30 °C and −5 °C, the signal of the fluid is quite weak and the liquid content rises slowly. The bound water is directly bound to the hydrogen bond of the macromolecular group, so the binding force is stronger and the fluidity of the water is weaker, as the attenuation rate is faster. Free water, on the other hand, is not affected by the structure, the fluidity

of the water is strong, and the attenuation rate is the slowest [39,40]. Therefore, different states of water can be distinguished based on the magnitude of the relaxation time. These three peaks can represent different water states, such as bound water, perturbed water, and free water, respectively. Thus, T_2 spectra are divided into three peaks, from left to right, P_1 , P_2 , and P_3 , where P_1 represents bound water, P_2 , varying in complexity, represents perturbed water, and P_3 represents free water. The pore size increases with increasing T_2 relaxation time.

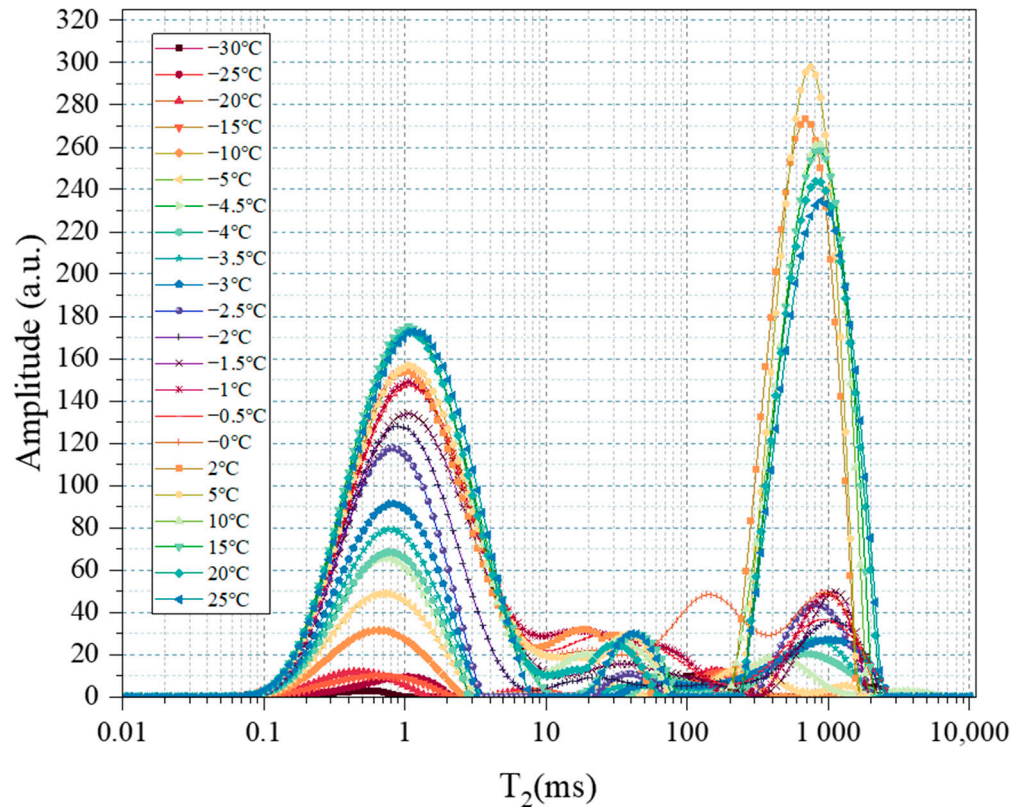


Figure 12. The T_2 relaxation time of NMRC experiment.

As can be seen from the 3D diagram (Figure 13), the bound water content increases as the temperature increases. The perturbed water starts to increase gradually and continuously at $-5\text{ }^\circ\text{C}$ and migrates through the pores. At $0\text{--}2\text{ }^\circ\text{C}$, the free water content increases significantly, indicating that the ice has completely melted into water.

Starting at $-5\text{ }^\circ\text{C}$, the signal changes significantly and water is transported into larger pores. P_3 (Figures 14 and 15) shows two small peaks, indicating that the water in the larger pore size is in a perturbation state. This shows that, below $-5\text{ }^\circ\text{C}$, water exists in the form of bound water (water film).

Between $-5\text{ }^\circ\text{C}$ and $0\text{ }^\circ\text{C}$, the bound water content continued to increase, and the signals of the P_2 and P_3 peaks were enhanced with the perturbation, and the perturbed water was transported in the pore space; meanwhile, there was no significant enhancement in the signal of the P_3 peak, suggesting that ice of the smaller pores melted first, and the freezing point decreased due to the influence of pore size, which was caused by the Gibbs–Thomson effect [41–44].

When the temperature is higher than $-5\text{ }^\circ\text{C}$ (Figure 16), the content and distribution of water in the pores of the sample change significantly. Therefore, $-5\text{ }^\circ\text{C}$ can be considered to be the freezing point boundary value for adsorbed water and capillary water in the sediment pores; this phenomenon corroborates the view of Razumova et al. and Jaeger et al. [45].

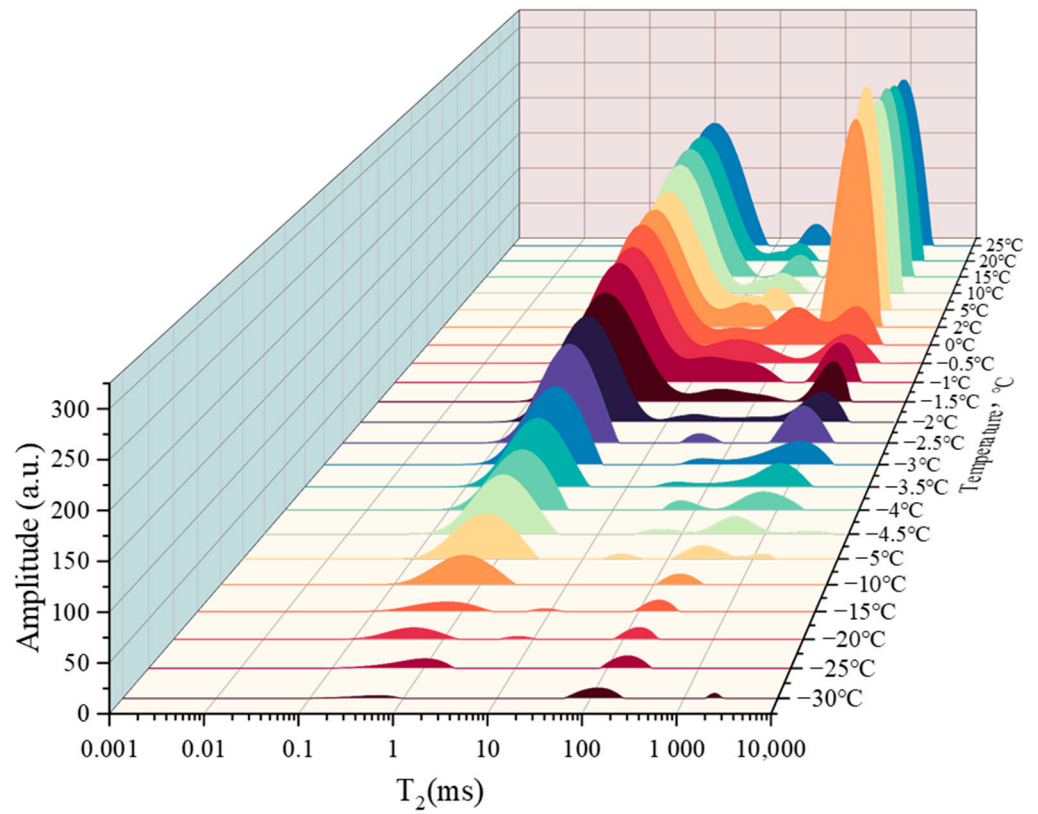


Figure 13. Three-dimensional plot of the peak amplitude of the T_2 spectrum as a function of temperature.

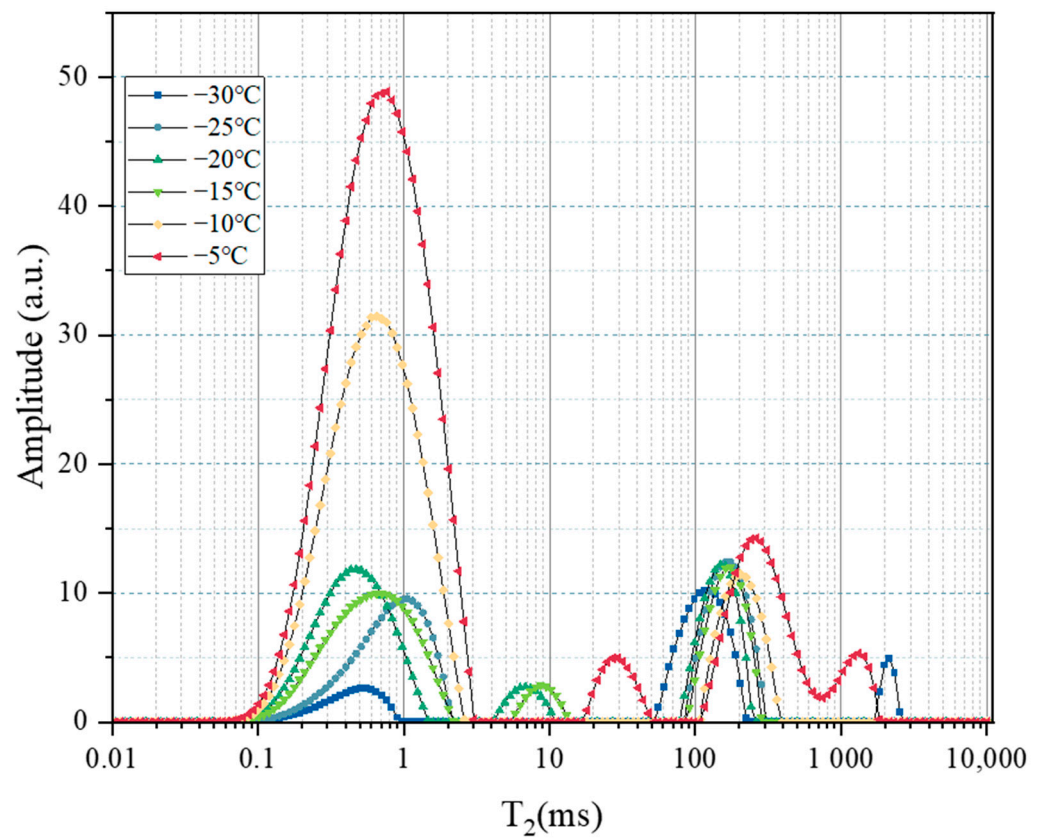


Figure 14. The T_2 spectrum of NMRC with temperature varies from $-30\text{ }^\circ\text{C}$ to $-5\text{ }^\circ\text{C}$.

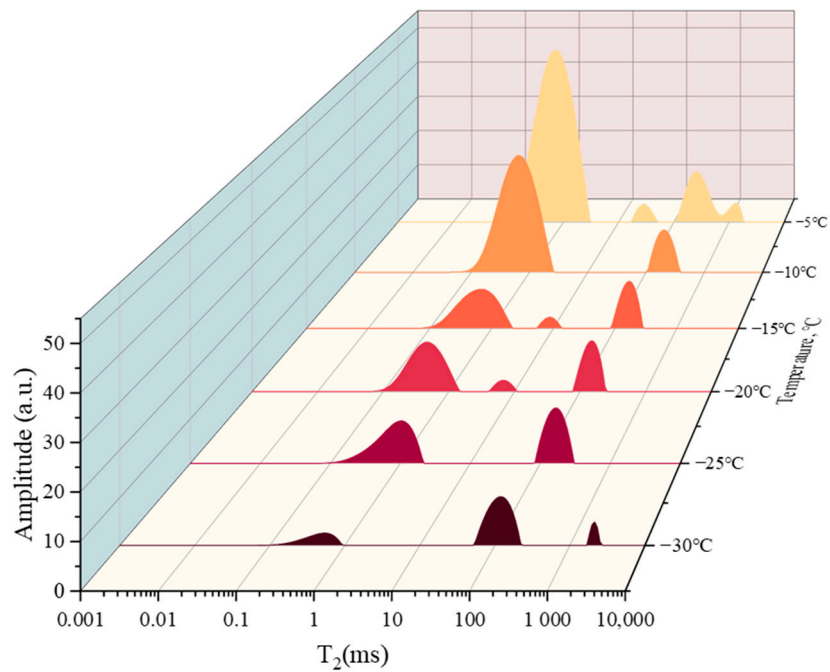


Figure 15. The 3D T₂ spectrum of NMRC with temperature varies from −30 °C to −5 °C.

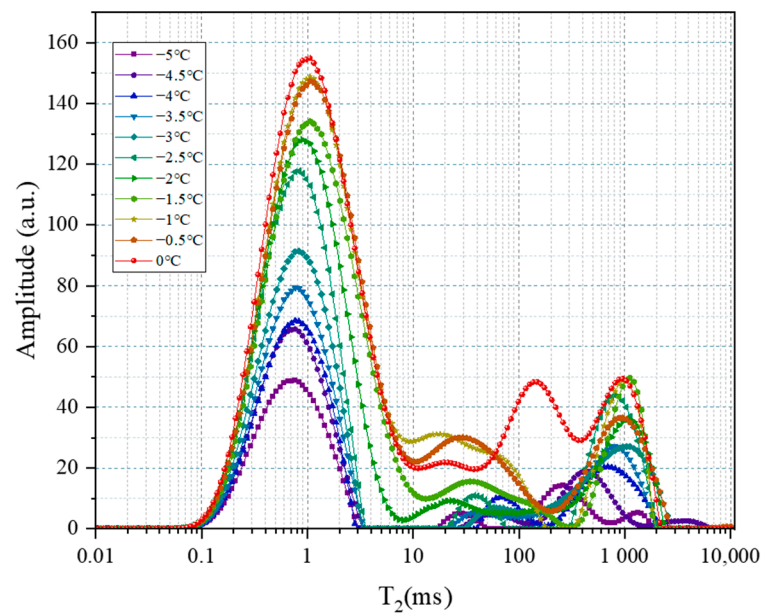


Figure 16. The T₂ spectrum of NMRC with temperature varies from −5 °C to 0 °C.

The pore size distribution is as follows:

The PSDs of the sample are shown in Figure 17. Pores in the 2–10 nm range contribute less to pore volume than those in the 10–100 nm range, and pores in the 9–10 nm range have the peak pore volume. The pore size ranges with a large pore volume contribution are 10–50 nm.

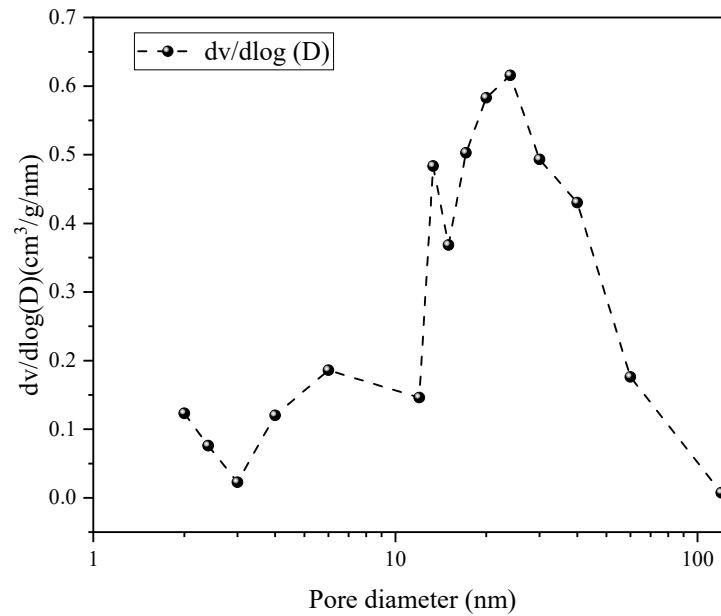


Figure 17. The PSDs of the hydrate-bearing Sample 58.

By calibrating with NMRC technology, the trend distribution map of the unfrozen water content was obtained (Figure 18). The PSDs of Samples 58 are shown in Figure 15. Among them, pore sizes in the range of 10–100 nm account for a relatively larger percent of the pore volume. Compared to the N₂GA method, NMRC can characterize a larger range of pore sizes, detect more closed pores, and calculate the water content in the pores (Figure 18).

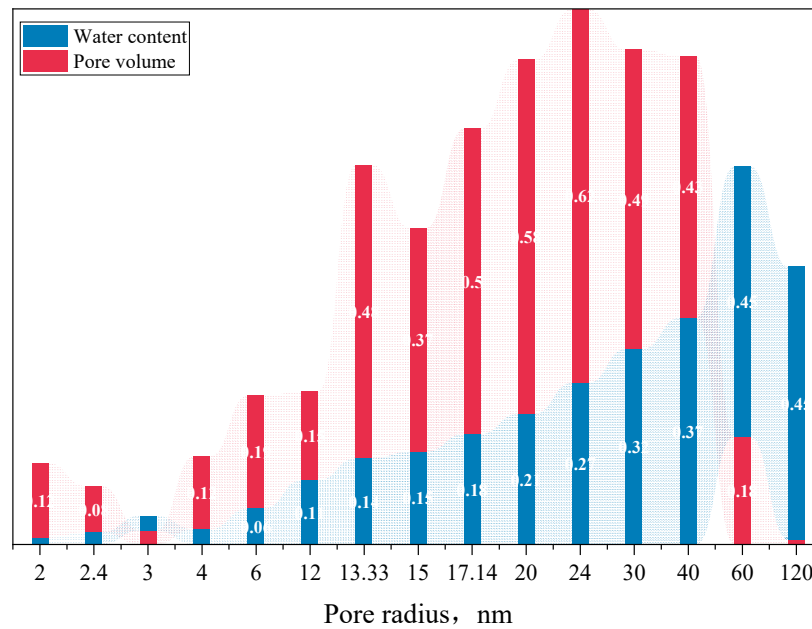


Figure 18. Schematic diagram of pore volume and water content variation with pore size.

4.3.3. Pore Volume (PV) and Surface Area (SSA)

PV and SSA can be used to study the storage space of natural gas and are a vital part of reservoir evaluation. In general, pores can be divided into macropores (>50 nm), mesopores (2–50 nm), and micropores (<2 nm). In this study, SSA can be obtained based on the BET model, PV can be obtained by the BJH model, and pore size distribution can be

obtained by the BJH or DFT model. Among them, the DFT model can be used to jointly characterize the PSDs of the samples from micropores to partial macropores.

The pore structure parameters are presented in Table 1. The values of the micropore surface area of samples are 76.232 m²/g and 64.751 m²/g, respectively. The pore volume of the micropores (pore size 2–50 nm) of the samples are 0.108 cc/g and 0.110 cc/g.

Table 1. Pore structure parameters of samples.

Sample	BET Surface Area (m ² /g)	BJH Pore Volume (cc/g)
58	76.232	0.108
68	64.751	0.110

4.3.4. Micrometer Scale Characterization—HPMI

The data of the HPMI method show that the radius of the pore throat in the KG Basin is concentrated in the nano-scale, with a few micron-scale pore throats. Among them, micro-scale pore throats have a greater permeability contribution than nano-scale pore throats.

The pore size distributions obtained by HPMI only represent the pore (or throats) that have the permeability contribution, and do not reflect the pore size distribution of the entire sample, and cannot distinguish between the pore and throat. Therefore, the combination of the CRMI and NMRC methods was used for further research.

The capillary pressure curves of mercury intrusion and extrusion are depicted in Figure 19, and their key parameters are listed in Table 2.

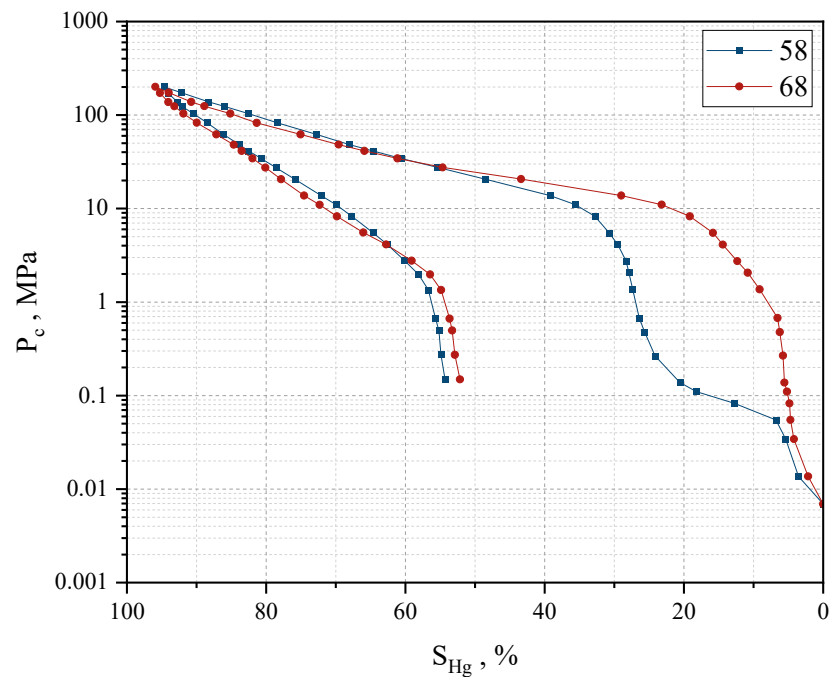


Figure 19. Capillary pressure curves of mercury intrusion and extrusion obtained by HPMI.

The parameters indicate that the permeability of Sample 58 and Sample 68 is quite different, at $160.8 \times 10^{-3} \mu\text{m}^2$ and $0.142 \times 10^{-3} \mu\text{m}^2$, respectively, but the porosity is similar (Table 2).

The throat radius shows that, although the median values of the two sample are the same, the maximum value of the throat was very different, with Sample 58 having a larger average throat radius of 2.937 μm , where the maximum throat radius could reach 13.368 μm ; meanwhile, Sample 68 had a nanometer average throat radius of only 0.114 μm and a maximum throat radius of 1.088 μm .

Table 2. Parameters of pore throat size in hydrate-bearing reservoir from HPMI.

Permeability	Porosity	Pore Throat Radius			Pore Throat Size Distribution		Permeability Distribution	
		Maximum	Average	Median	Peak Position	Peak Value	Peak Position	Peak Value
$10^{-3} \mu\text{m}^2$	(%)	R_a	R_p	R_{50}	(μm)	(%)	(μm)	(%)
K	φ	R_a	R_p	R_{50}	R_v	R_m	R_f	F_m
160.8	36.04	13.368	2.937	0.035	0.025	10.769	10.000	63.510
0.142	31.44	1.088	0.114	0.031	0.025	16.868	0.630	59.533

The pore throat is distributed over a wide range, from the nanometer to micrometer scale, with the larger pore throat providing permeability (Figure 20). The permeability contribution of Sample 58 corresponds to the pore size distribution ranging from 2–10 μm , so the permeability contribution of Sample 68 corresponds to the pore size distribution ranging from 0.2–1 μm . In Samples 58 and 68, the pore sizes with the strongest permeability were 10 μm and 0.6 μm , respectively.

R_v and R_m , respectively, mean the peak position and peak value of the PSD. The R_v values of the two sample are the same: Sample 68 has a higher value of R_m than Sample 58.

R_f represents the peak position of the permeability distribution, while F_m represents the peak value of the permeability distribution. In Sample 58, the pore throat radius of 10 μm contributes the most permeability, while, in Sample 68, the pore throat radius of 0.63 μm contributes the most permeability. This is the reason why the porosity of the two sample is the same, but the permeability is quite different.

The parameters of the pore throat structure from HPMI can be seen in Table 3. The overall sorting coefficients show that the overall pore throat sorting is good for both samples; thus, the relative sorting coefficients need to be analyzed. The relative sorting coefficient is used to characterize the uniformity of the pore size, with Sample 58 having a smaller relative sorting coefficient of 1.713, indicating that the pore size of the samples is not uniform, whereas the relative sorting coefficient of Sample 68 is larger at 36.264, indicating that the pore size of the samples is more uniform.

Table 3. Parameters of pore throat structure in hydrate-bearing reservoir from HPMI.

Sorting Factor	Skewness	Kurtosis	Mean Radius (μm)	Structural Coefficient	Relative Sorting Coefficient	Characteristic Structural Parameters	Homogeneity Coefficient
S_p	S_{kp}	K_p	D_m	Φ	D	$1/D\Phi$	α
4.273	−0.494	0.622	2.495	2.417	1.713	0.242	0.220
2.184	−0.146	1.312	0.060	3.622	36.264	0.008	0.105

The sorting coefficient is also reflected in the structural characteristic parameters. There is a close relationship between the structural characteristic parameters and the relative permeability: the larger the structural characteristic parameters, the better the relative sorting of the pores. When the difference in pore size is large, the relative sorting is poor, the pore size occupied by the wetting phase and the non-wetting phase is vastly different, the non-wetting phase preferentially occupies the large pore space, which inevitably results in a substantial increase in the relative permeability of the non-wetting phase, and then the saturation of the intersection point is shifted to the left.

The structure coefficient φ indicates the degree of seepage and circuitous flow of the fluid in the pores, and the larger the φ value, the stronger the degree of pore bending and meandering. The pore curvature of Sample 68 is greater than that of Sample 58.

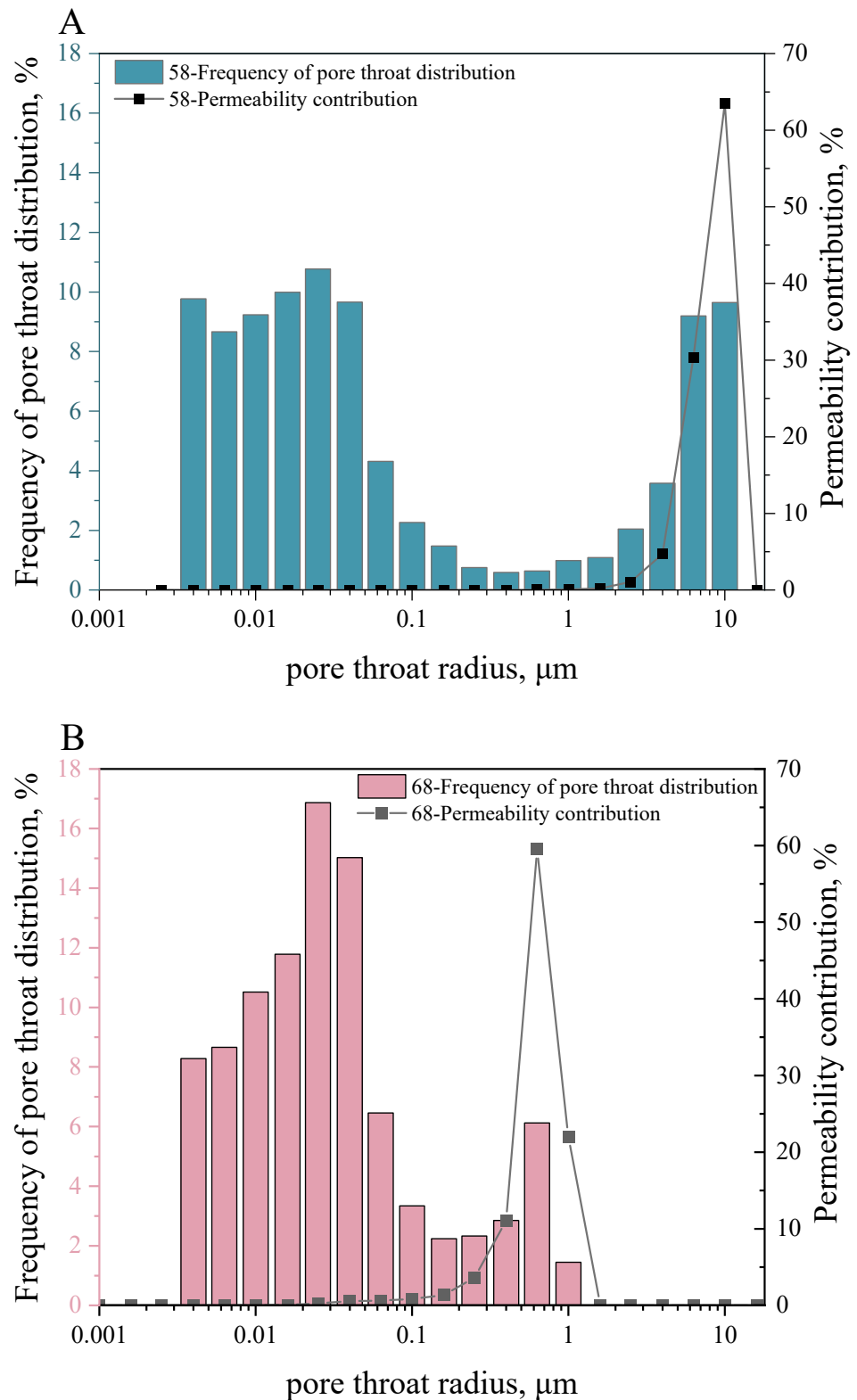


Figure 20. The pore throat size distribution and its contribution to the permeability of Sample 58 (A) and Sample 68 (B) obtained by HPMI.

Skewness is a measure of the asymmetry of the pore throat size distribution. The S_{kp} value varies between ± 1 , i.e., $-1 \leq S_{kp} \leq 1$; with $S_{kp} = 0$, indicating that the pore distribution curve is symmetrical, $S_{kp} > 0$ for coarse skewness, and $S_{kp} < 0$ for fine skewness.

Samples 58 and 68 have fine skewness; i.e., the pore throat size distribution is biased in favor of fine pore throats.

The kurtosis measures of the steepness of the frequency curve, i.e., the ratio of the throat diameters of the two tails (anterior and posterior) of the frequency curve distribution to the center of the curve, show the following: $K_p = 1$ means the pore distribution curve is normally distributed, $K_p > 1$ is the peak curve, and $K_p < 1$ is a flat or multimodal curve. The kurtosis value of the Sample 58 is smaller than that of the Sample 68.

The homogeneity coefficient α indicates the degree of concentration of the main infiltration pore channels. The homogeneity coefficients are similar for both samples, with Sample 58 having a higher concentration of percolation pore channels.

The homogeneity coefficient α indicates the concentration of the main percolation channels. The homogeneity coefficient was similar for both samples; Sample 58 had a higher concentration of percolation pores and channels.

4.3.5. Micrometer Scale Characterization—CRMI

Sample 58 showed a steady increase in the mercury saturation increment (Figure 21A), while Sample 68 showed an abnormally high value of mercury saturation at 3 μm , with high mercury saturation below 1 μm and above 5 μm in Figure 21B, corroborating the findings from the HPMI experiments; Sample 58 has a higher concentration of percolation pores and channels.

The parameters of CRMI, such as the pore/throat radius distribution (Figures 22 and 23) and the pore/throat radius ratio distribution (Figure 24), can accurately reflect the microstructure characteristics of the sediment.

The pore radius of Sample 58 is concentrated in the range of 100–300 μm , with the peak occurring in the interval around 150 μm (Figure 22A). The pore radius of Sample 68 is mainly concentrated within 100 μm , and the pore volume decreases with increasing pore radius, with the peak occurring in the range of 50 μm (Figure 22B).

The throat radius of Sample 58 was distributed within 30 μm and the pore volume decreased with increasing throat radius (Figure 23A), and the throat radius of Sample 68 was distributed within 25 μm , where the throat with a radius of less than 15 μm accounted for the majority of the throat volume; the throat with a radius of 5 μm contributes to the largest volume of the throat (Figure 23B).

Figure 24 shows the distribution frequencies of the ratio of the pore radius to throat radius, respectively. The peak of the distribution frequency of Sample 68 was greater than that of Sample 58, which was mainly distributed within 200 μm and Sample 68 was mainly distributed within 300 μm .

Above all, Samples 58 and 68 all developed nanopores, the mineral distribution was relatively scattered, and they were rich in paleontological shells such as foraminifera, among which Sample 68 had more pyrite content, and abundant pyrite framboid was observed, which made the intergranular pore develop and provide more nanopores. Sample 58 has a high concentration of pore and throat, high pore connectivity, low pore curvature, and pores with a diameter of 10 μm contributing to the main permeability, with an average pore radius of 2.495 μm , whereas Sample 68 has a poor pore connectivity, high curvature, and pores with a diameter of 1 μm contributing to the main permeability, with an average pore diameter of 60 nm, which explains the obvious difference in permeability between the two samples.

The pore characterization of reservoirs in the KG Basin in this paper has made significant contributions to the evaluation of resource potential, the study of accumulation mechanism, and the support of engineering technology.

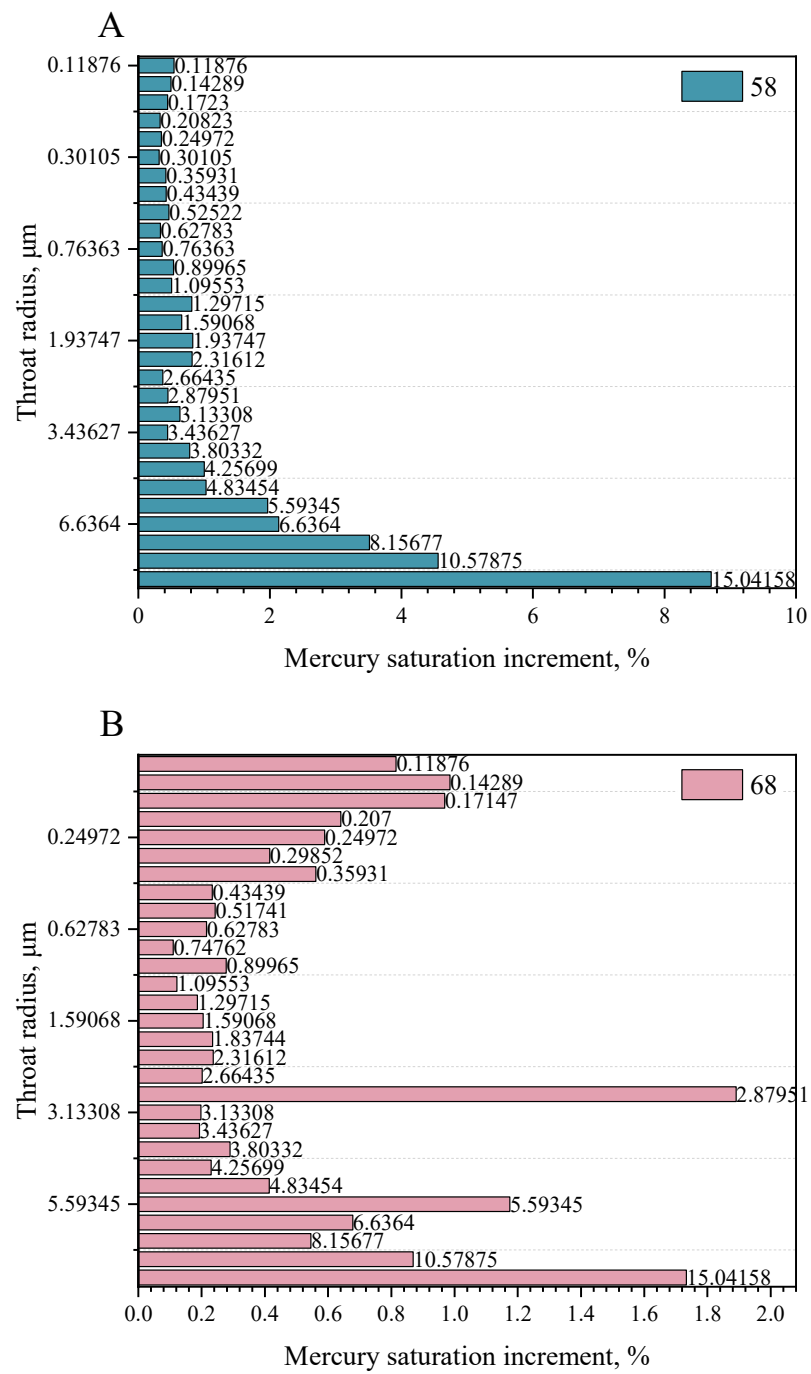


Figure 21. Schematic of mercury saturation as a function of constant velocity mercury pressing: (A,B) variation of throat radius with incremental mercury saturation for Samples 58 and 68.

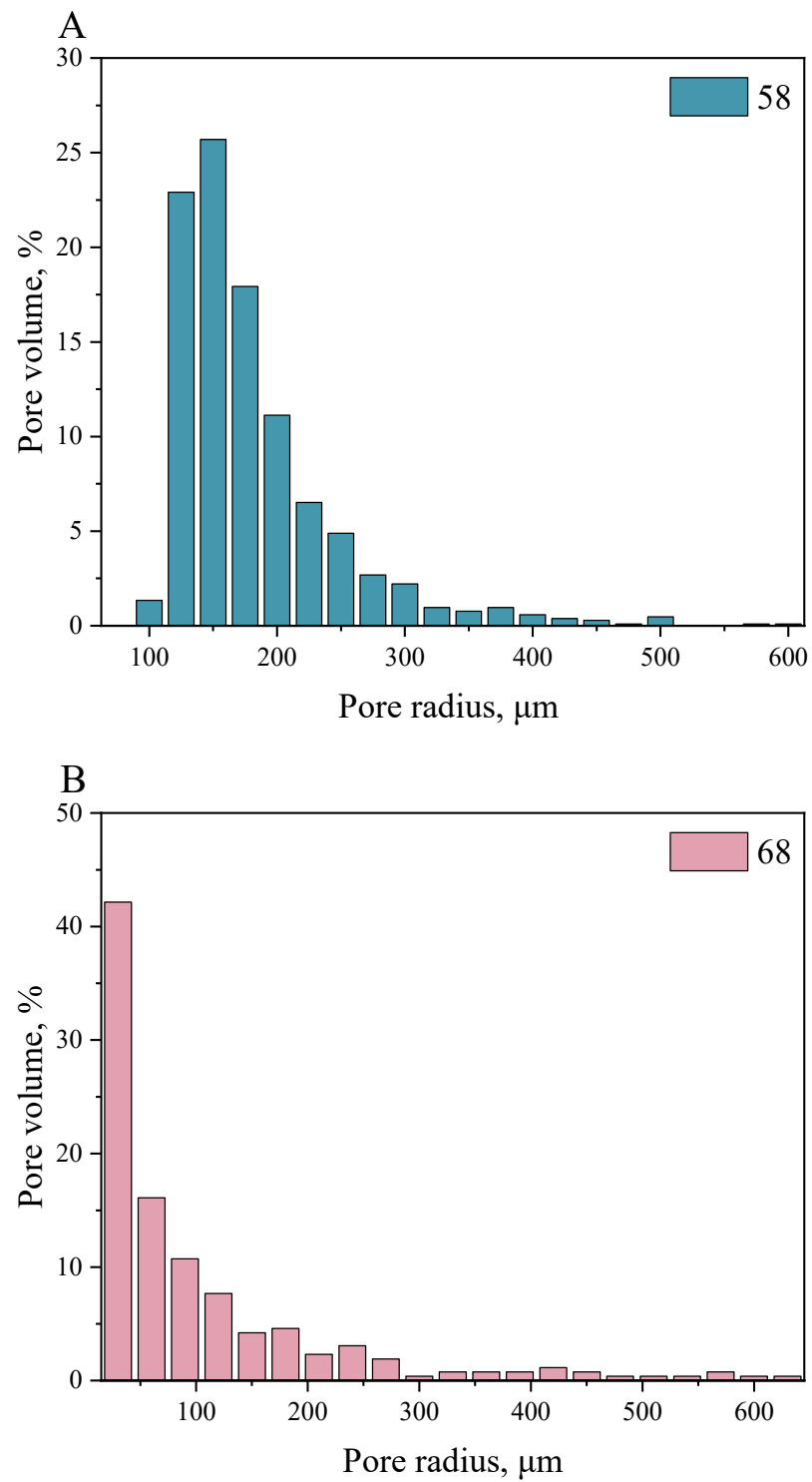


Figure 22. Schematic diagram of pore and throat radius for CRMI: (A,B) schematic diagram of pore volume variation with pore radius for Samples 58 and 68.

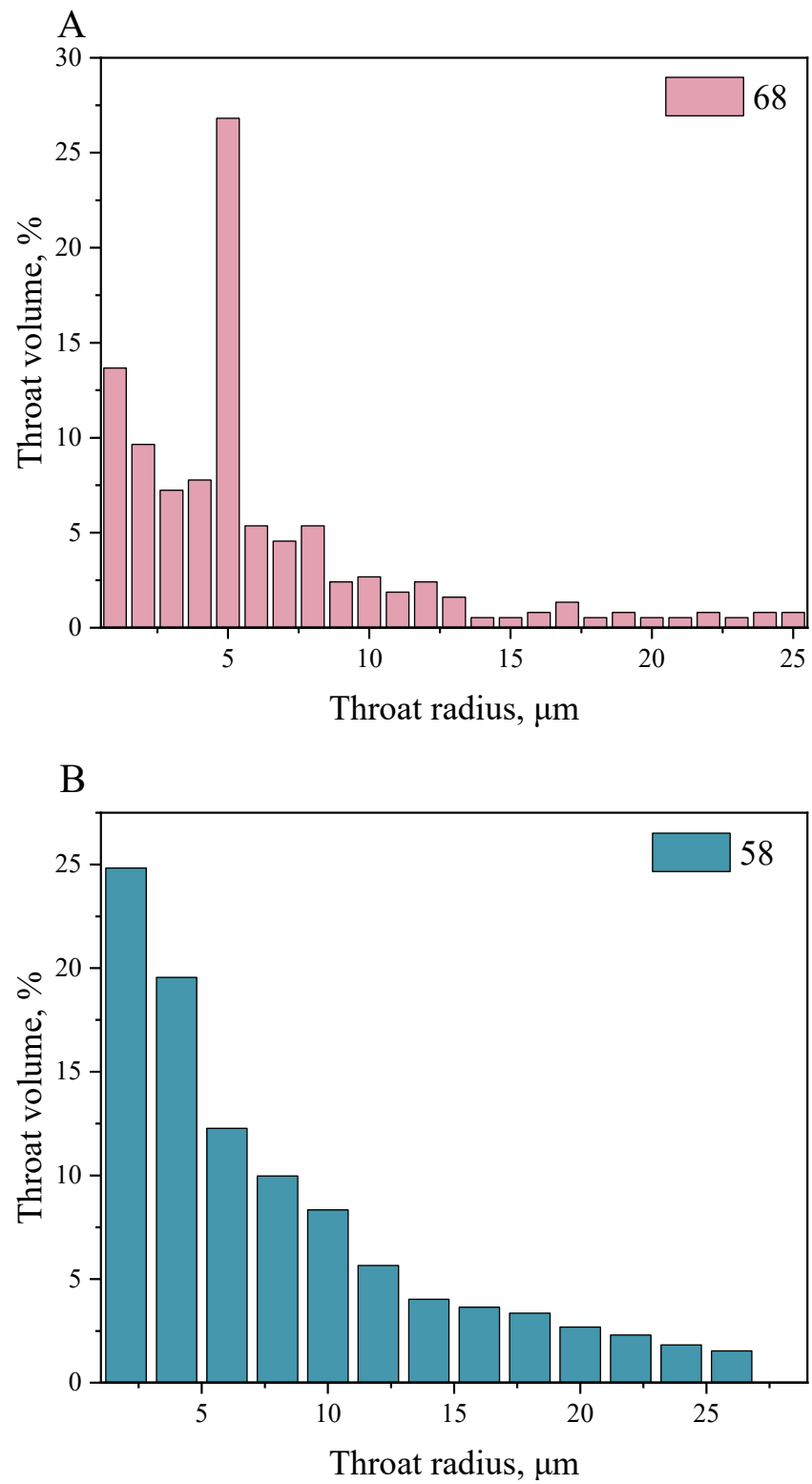


Figure 23. Schematic diagram of pore and throat radius for CRMI: (A,B) schematic diagram of the variation of throat volume with throat radius for Samples 58 and 68.

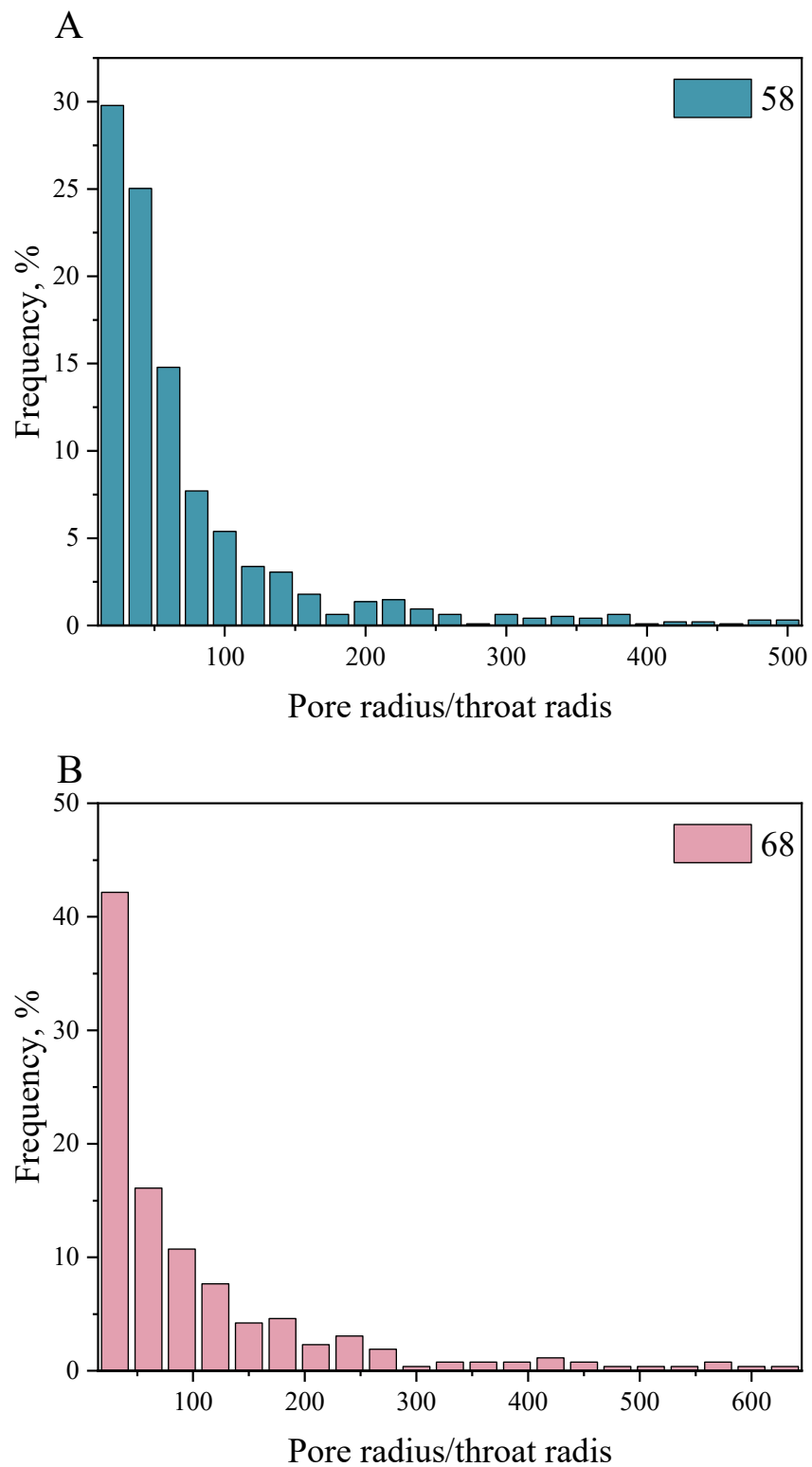


Figure 24. Schematic diagram of pore and throat radius for CRMI: (A,B) frequency diagrams of the ratio of pore radius to throat radius for Samples 58 and 68.

Understanding the pore structure of sediments can help optimize engineering and technical measures in drilling, completion, and production, improving production efficiency and safety.

In addition, an accurate assessment of gas hydrate reserves in the KG Basin is of great significance for India’s energy strategy. As potential clean energy, the development and

utilization of natural gas hydrate will help alleviate the energy shortage and promote the optimization and sustainable development of the energy structure.

Moreover, the extraction of gas hydrates may have environmental impacts, such as methane releases and seabed geological hazards. Through pore characterization, the environmental impact of mining activities can be assessed, and effective environmental protection measures can be formulated to ensure the safe conduct of mining activities.

In terms of future work, it is suggested that the pore characterization results should be combined with numerical simulation techniques to simulate the formation, distribution, and evolution of gas hydrates in sediment pores. This will help to understand the accumulation mechanism of gas hydrates and provide more scientific guidance for their exploration and exploitation. Secondly, in the process of gas hydrate exploration and exploitation, attention could be paid to environmental protection and sustainable development, and, in the future, the research and implementation of environmental protection measures can be strengthened to ensure that the information of the reservoir pore system can promote the safe conduct of mining activities and minimize the impact on the environment. At the same time, the joint development and utilization mode of natural gas hydrates and other clean energy in the same reservoir can be explored to promote the optimization and sustainable development of the energy structure.

5. Conclusions

This study aims to apply the characterization method of unconventional reservoirs to the sediment pore characterization of hydrate-bearing reservoirs, and integrate methods to obtain various information about pores, such as pore size distribution, porosity, average pore size, pore volume, pore specific surface area, and other features, and also the three-dimensional spatial information of pores.

The results show that the nanoscale characterization methods include N₂GA and NMRC. The NMRC method measured a much larger total pore volume than the N₂GA method, which is presumed to be due to the closed pores, while N₂GA did not measure the closed-pore volume, resulting in a large variation in the total pore volume comparison results.

In terms of micron-scale characterization, HMPI highlights the permeability contribution of the pore throat, while CRMI mainly focuses on the distinction between the pore and larynx. The advantage of CTS is in observing the distribution of minerals, and SEM is suitable for studying intergranular pores.

The pore types of hydrate-bearing reservoirs in the KG Basin are complex, and the pore morphology is diverse, including closed pores, open pores, ink-bottle pores, etc., and foraminifera shells and diatom shells provide storage space; in addition, the connectivity between the pores is poor, with 4–20 μm pores contributing the most to permeability.

Author Contributions: Literature search, W.G.; study design, W.G., H.L.; data analysis, W.G.; data interpretation, W.G., H.Y., X.L.; writing—original draft preparation, W.G.; writing—review and editing, W.G., H.Y., X.L., H.L.; supervision, H.L.; project administration, H.L.; funding acquisition, H.L. All authors have read and agreed to the published version of the manuscript.

Funding: This study was funded by the DD20230063 and DD20221703 from the China Geological Survey and the Guangdong Major Project of Basic and Applied Basic Research (No.2020B0301030003).

Institutional Review Board Statement: Not applicable.

Informed Consent Statement: Not applicable.

Data Availability Statement: The raw data supporting the conclusions of this article will be made available by the authors on request.

Conflicts of Interest: The authors declare no conflicts of interest.

References

1. Lijith, K.P.; Srinivasa Rao, R.; Narain Singh, D. Investigations on the influence of wellbore configuration and permeability anisotropy on the gas production from a turbidite hydrate reservoir of KG Basin. *Fuel* **2022**, *317*, 123562. [[CrossRef](#)]
2. Chaturvedi, E.; Maiti, M.; Laik, S.; Mandal, A. Mineralogical and structural characterization of the sediments of Krishna Godavari and Mahanadi Basin and their influences on hydrate formation kinetics. *Adv. Powder Technol.* **2021**, *32*, 1247–1263. [[CrossRef](#)]
3. Bhawangirkar, D.R.; Nair, V.C.; Prasad, S.K.; Sangwai, J.S. Natural Gas Hydrates in the Krishna-Godavari Basin Sediments under Marine Reservoir Conditions: Thermodynamics and Dissociation Kinetics using Thermal Stimulation. *Energy Fuels* **2021**, *35*, 8685–8698. [[CrossRef](#)]
4. Liu, Z.; Chen, L.; Wang, Z.; Gao, Y.; Wang, J.; Yu, C.; Sun, B. Hydrate phase equilibria in natural sediments: Inhibition mechanism and NMR-based prediction method. *Chem. Eng. J.* **2023**, *452*, 139447. [[CrossRef](#)]
5. Bian, H.; Ai, L.; Hellgardt, K.; Maitland, G.C.; Heng, J.Y.Y. Phase Behaviour of Methane Hydrates in Confined Media. *Crystals* **2021**, *11*, 201. [[CrossRef](#)]
6. Zhang, Y.; Wang, T.; Li, X.; Yan, K.; Wang, Y.; Chen, Z. Decomposition behaviors of methane hydrate in porous media below the ice melting point by depressurization. *Chin. J. Chem. Eng.* **2019**, *27*, 2207–2212. [[CrossRef](#)]
7. Lee, S.; Seo, Y. Experimental measurement and thermodynamic modeling of the mixed CH₄ + C₃H₈ clathrate hydrate equilibria in silica gel pores: Effects of pore size and salinity. *Langmuir* **2010**, *26*, 9742–9748. [[CrossRef](#)]
8. Liu, H.; Zhan, S.; Guo, P.; Fan, S.; Zhang, S. Understanding the characteristic of methane hydrate equilibrium in materials and its potential application. *Chem. Eng. J.* **2018**, *349*, 775–781. [[CrossRef](#)]
9. Fang, B.; Lü, T.; Li, W.; Moulton, O.A.; Vlugt, T.J.H.; Ning, F. Microscopic insights into poly- and mono-crystalline methane hydrate dissociation in Na-montmorillonite pores at static and dynamic fluid conditions. *Energy* **2024**, *288*, 129755. [[CrossRef](#)]
10. Yoneda, J.; Oshima, M.; Kida, M.; Kato, A.; Konno, Y.; Jin, Y.; Jang, J.; Waite, W.F.; Kumar, P.; Tenma, N. Permeability variation and anisotropy of gas hydrate-bearing pressure-core sediments recovered from the Krishna–Godavari Basin, offshore India. *Mar. Pet. Geol.* **2019**, *108*, 524–536. [[CrossRef](#)]
11. Oshima, M.; Suzuki, K.; Yoneda, J.; Kato, A.; Kida, M.; Konno, Y.; Muraoka, M.; Jin, Y.; Nagao, J.; Tenma, N. Lithological properties of natural gas hydrate-bearing sediments in pressure-cores recovered from the Krishna–Godavari Basin. *Mar. Pet. Geol.* **2019**, *108*, 439–470. [[CrossRef](#)]
12. Yamamoto, K. Overview and introduction: Pressure core-sampling and analyses in the 2012–2013 MH21 offshore test of gas production from methane hydrates in the eastern Nankai Trough. *Mar. Pet. Geol.* **2015**, *66*, 296–309. [[CrossRef](#)]
13. Daigle, H.; Johnson, A. Combining Mercury Intrusion and Nuclear Magnetic Resonance Measurements Using Percolation Theory. *Transp. Porous Media* **2015**, *111*, 669–679. [[CrossRef](#)]
14. Daigle, H.; Dugan, B. Pore size controls on the base of the methane hydrate stability zone in the Kumano Basin, offshore Japan. *Geophys. Res. Lett.* **2014**, *41*, 8021–8028. [[CrossRef](#)]
15. Vasheghani Farahani, M.; Guo, X.; Zhang, L.; Yang, M.; Hassanpouryouzband, A.; Zhao, J.; Yang, J.; Song, Y.; Tohidi, B. Effect of thermal formation/dissociation cycles on the kinetics of formation and pore-scale distribution of methane hydrates in porous media: A magnetic resonance imaging study. *Sustain. Energy Fuels* **2021**, *5*, 1567–1583. [[CrossRef](#)]
16. Hassanpouryouzband, A.; Joonaki, E.; Vasheghani Farahani, M.; Takeya, S.; Ruppel, C.; Yang, J.; English, N.J.; Schicks, J.M.; Edlmann, K.; Mehrabian, H.; et al. Gas hydrates in sustainable chemistry. *Chem. Soc. Rev.* **2020**, *49*, 5225–5309. [[CrossRef](#)] [[PubMed](#)]
17. Kocherla, M.; Ray, D.; Satyanarayanan, M.; João, H.M.; Sojan, C. Trace and rare earth element systematics of cold-seep carbonates from the Krishna-Godavari basin: A comparison between isotopically distinct carbonate deposits. *Mar. Chem.* **2024**, *259*, 104363. [[CrossRef](#)]
18. Singh, A.; Ojha, M. Machine learning in the classification of lithology using downhole NMR data of the NGHP-02 expedition in the Krishna-Godavari offshore Basin, India. *Mar. Pet. Geol.* **2022**, *135*, 105443. [[CrossRef](#)]
19. Peketi, A.; Mazumdar, A.; Sawant, B.; Manaskanya, A.; Zatale, A. Biogeochemistry and trophic structure of a cold seep ecosystem, offshore Krishna-Godavari basin (east coast of India). *Mar. Pet. Geol.* **2022**, *138*, 105542. [[CrossRef](#)]
20. Nukapothula, S.; Chen, C.; Yunus, A.P. Seasonal sediment plumes in the Krishna-Godavari basin using satellite observations. *Deep Sea Res. Part I Oceanogr. Res. Pap.* **2022**, *188*, 103850. [[CrossRef](#)]
21. Rehitha, T.V.; Madhu, N.V.; Vipindas, P.V.; Vineetha, G.; Ullas, N.; Muraleedharan, K.R.; Nair, M. Influence of oil and gas exploration activities on the macrobenthic community structure of the Krishna-Godavari basin (Ravva coast), Western Bay of Bengal. *Cont. Shelf Res.* **2021**, *224*, 104463. [[CrossRef](#)]
22. Chatterjee, R.; Singha, D.K.; Ojha, M.; Sen, M.K.; Sain, K. Porosity estimation from pre-stack seismic data in gas-hydrate bearing sediments, Krishna-Godavari basin, India. *J. Nat. Gas Sci. Eng.* **2016**, *33*, 562–572. [[CrossRef](#)]
23. Qiao, J.; Zeng, J.; Jiang, S.; Feng, S.; Feng, X.; Guo, Z.; Teng, J. Heterogeneity of reservoir quality and gas accumulation in tight sandstone reservoirs revealed by pore structure characterization and physical simulation. *Fuel* **2019**, *253*, 1300–1316. [[CrossRef](#)]
24. Mazumdar, A.; Kocherla, M.; Carvalho, M.A.; Peketi, A.; Joshi, R.K.; Mahalaxmi, P.; Joao, H.M.; Jisha, R. Geochemical characterization of the Krishna–Godavari and Mahanadi offshore basin (Bay of Bengal) sediments: A comparative study of provenance. *Mar. Pet. Geol.* **2015**, *60*, 18–33. [[CrossRef](#)]
25. Xie, S.; Cheng, Q.; Ling, Q.; Li, B.; Bao, Z.; Fan, P. Fractal and multifractal analysis of carbonate pore-scale digital images of petroleum reservoirs. *Mar. Pet. Geol.* **2010**, *27*, 476–485. [[CrossRef](#)]

26. Liu, X.; Nie, B. Fractal characteristics of coal samples utilizing image analysis and gas adsorption. *Fuel* **2016**, *182*, 314–322. [[CrossRef](#)]
27. Liu, J.; Zhang, C.; Jiang, Y.; Hou, S. Investigation on pore structure characteristics of ultra-tight sandstone reservoirs in the upper Triassic Xujiache Formation of the northern Sichuan Basin, China. *Mar. Pet. Geol.* **2022**, *138*, 105552. [[CrossRef](#)]
28. Qin, Y.; Yao, S.; Xiao, H.; Cao, J.; Hu, W.; Sun, L.; Tao, K.; Liu, X. Pore structure and connectivity of tight sandstone reservoirs in petroleum basins: A review and application of new methodologies to the Late Triassic Ordos Basin, China. *Mar. Pet. Geol.* **2021**, *129*, 105084. [[CrossRef](#)]
29. Fleury, M.; Chevalier, T.; Jorand, R.; Jolivet, I.; Nicot, B. Oil-water pore occupancy in the Vaca Muerta source-rocks by NMR cryoporometry. *Microporous Mesoporous Mater.* **2021**, *311*, 110680. [[CrossRef](#)]
30. Zhao, Y.; Peng, L.; Liu, S.; Cao, B.; Sun, Y.; Hou, B. Pore structure characterization of shales using synchrotron SAXS and NMR cryoporometry. *Mar. Pet. Geol.* **2019**, *102*, 116–125. [[CrossRef](#)]
31. Yin, T.; Liu, D.; Cai, Y.; Zhou, Y. Methane adsorption constrained by pore structure in high-rank coals using FESEM, CO₂ adsorption, and NMRC techniques. *Energy Sci. Eng.* **2019**, *7*, 255–271. [[CrossRef](#)]
32. Zhou, T.; Wu, C.; Shi, Z.; Wang, J.; Zhu, W.; Yuan, B.; Yang, D. Multi-Scale Quantitative Characterization of Pore Distribution Networks in Tight Sandstone by integrating FE-SEM, HPMTI, and NMR with the Constrained Least Squares Algorithm. *Energies* **2019**, *12*, 3514. [[CrossRef](#)]
33. Zhang, M.; Fu, X. Characterization of pore structure and its impact on methane adsorption capacity for semi-anthracite in Shizhuangnan Block, Qinshui Basin. *J. Nat. Gas Sci. Eng.* **2018**, *60*, 49–62. [[CrossRef](#)]
34. Zhang, H.; Shen, J.; Wang, G.; Li, K.; Fang, X. Experimental study on the effect of high-temperature nitrogen immersion on the nanoscale pore structure of different lithotypes of coal. *Energy* **2023**, *284*, 128596. [[CrossRef](#)]
35. Xiong, J.; Liu, X.; Liang, L. Experimental study on the pore structure characteristics of the Upper Ordovician Wufeng Formation shale in the southwest portion of the Sichuan Basin, China. *J. Nat. Gas Sci. Eng.* **2015**, *22*, 530–539. [[CrossRef](#)]
36. Wang, Z.; Hao, C.; Wang, X.; Wang, G.; Ni, G.; Cheng, Y. Effects of micro-mesopore structure characteristics on methane adsorption capacity of medium rank coal. *Fuel* **2023**, *351*, 128910. [[CrossRef](#)]
37. Wang, X.; Wang, M.; Li, J.; Shao, H.; Deng, Z.; Wu, Y. Thermal maturity: The controlling factor of wettability, pore structure, and oil content in the lacustrine Qingshankou shale, Songliao Basin. *J. Pet. Sci. Eng.* **2022**, *215*, 110618. [[CrossRef](#)]
38. Wang, X.; Geng, J.; Zhang, D.; Xiao, W.; Chen, Y.; Zhang, H. Influence of sub-supercritical CO₂ on pore structure and fractal characteristics of anthracite: An experimental study. *Energy* **2022**, *261*, 125115. [[CrossRef](#)]
39. Yu, S.; Bo, J.; Ming, L.; Chenliang, H.; Shaochun, X. A review on pore-fractures in tectonically deformed coals. *Fuel* **2020**, *278*, 118248. [[CrossRef](#)]
40. Zang, Q.; Liu, C.; Awan, R.S.; Yang, X.; Li, G.; Wu, Y.; Lu, Z.; Feng, D. Occurrence characteristics of the movable fluid in heterogeneous sandstone reservoir based on fractal analysis of NMR data: A case study of the Chang 7 Member of Ansai Block, Ordos Basin, China. *J. Pet. Sci. Eng.* **2022**, *214*, 110499. [[CrossRef](#)]
41. Brunelli, D.N.; Skodje, R.T. Kinetics of multicomponent nanosize clusters on solid surfaces. *Langmuir* **2003**, *19*, 7130–7140. [[CrossRef](#)]
42. Sliwiska-Bartkowiak, M.; Dudziak, G.; Sikorski, R.; Gras, R.; Radhakrishnan, R.; Gubbins, K.E. Melting/freezing behavior of a fluid confined in porous glasses and MCM-41: Dielectric spectroscopy and molecular simulation. *J. Chem. Phys.* **2001**, *114*, 950–962. [[CrossRef](#)]
43. Sliwiska-Bartkowiak, M.; Jazdzewska, M. Melting behavior of bromobenzene within carbon nanotubes. *J. Chem. Eng. Data* **2010**, *55*, 4183–4189. [[CrossRef](#)]
44. Coasne, B.; Czwartos, J.; Sliwiska-Bartkowiak, M.; Gubbins, K.E. Effect of pressure on the freezing of pure fluids and mixtures confined in nanopores. *J. Phys. Chem. B* **2009**, *113*, 13874–13881. [[CrossRef](#)] [[PubMed](#)]
45. Jaeger, F.; Bowe, S.; Van As, H.; Schaumann, G.E. Evaluation of ¹H NMR relaxometry for the assessment of pore-size distribution in soil samples. *Eur. J. Soil Sci.* **2009**, *60*, 1052–1064. [[CrossRef](#)]

Disclaimer/Publisher’s Note: The statements, opinions and data contained in all publications are solely those of the individual author(s) and contributor(s) and not of MDPI and/or the editor(s). MDPI and/or the editor(s) disclaim responsibility for any injury to people or property resulting from any ideas, methods, instructions or products referred to in the content.